U.S. Department
of Transportation
**National Highway
Traffic Safety
Administration**

NHTSA

DOT HS 813 230

March 2022

Propagation Mitigation Testing Procedures, Modeling, and Analysis

DISCLAIMER

This publication is distributed by the U.S. Department of Transportation, National Highway Traffic Safety Administration, in the interest of information exchange. The opinions, findings and conclusions expressed in this publication are those of the authors and not necessarily those of the Department of Transportation or the National Highway Traffic Safety Administration. The United States Government assumes no liability for its contents or use thereof. If trade or manufacturers' names are mentioned, it is only because they are considered essential to the object of the publication and should not be construed as an endorsement. The United States Government does not endorse products or manufacturers.

NOTE: This report is published in the interest of advancing motor vehicle safety research. While the report may provide results from research or tests using specifically identified motor vehicle models, it is not intended to make conclusions about the safety performance or safety compliance of those motor vehicles, and no such conclusions should be drawn.

Suggested APA Format Citation:

Lamb, J., Kim, J., Kurzawski, A., Yang, C., Hewson, J., Mallarapu, A., Torres-Castro, L., Santhanagopalan, S., & Boudouris, B. (2022, March). *Propagation mitigation testing procedures, modeling, and analysis* (Report No. DOT HS 813 230). National Highway Traffic Safety Administration.

Technical Report Documentation Page

1. Report No. DOT HS 813 230	2. Government Accession No.	3. Recipient's Catalog No.
4. Title and Subtitle Propagation Mitigation Testing Procedures, Modeling, and Analysis		5. Report Date March 2022 6. Performing Organization Code
7. Authors Joshua Lamb, Jinyong Kim, Andrew Kurzawski, Chuanbo Yang, John Hewson, Anudeep Mallarapu, Loraine Torres-Castro, Shriram Santhanagopalan, Bryan Boudouris		8. Performing Organization Report No.
9. Performing Organization Name and Address Sandia National Laboratories P.O. Box 5800 Albuquerque, NM 87185		10. Work Unit No. (TRAIS) 11. Contract or Grant No. DOT IAG 18-2082
12. Sponsoring Agency Name and Address National Highway Traffic Safety Administration 1200 New Jersey Avenue SE Washington, DC 20590		13. Type of Report and Period Covered Final Report 14. Sponsoring Agency Code
15. Supplementary Notes		

16. Abstract

This work explores propagation mitigation in packs of lithium ion pouch cells commonly used in large electric vehicles. Sub-assemblies were constructed of three cells wired in series used to build the full test pack by wiring three of the sub-assemblies together in parallel. Abuse tests were then used to initiate failure within a single cell in either the sub-assembly or pack. In this work, we developed a numerical model to capture damage propagation within lithium ion cells and modules in which thermal runaway is triggered using different initiation methods. The interplay of three parameters for passive thermal management on thermal runaway mitigation was numerically studied, including thermal mass of metallic inserts, thermal contact resistance between components, and cooling rate. Based on these results, we found that connecting metallic inserts between cells instead of using separate metallic inserts between cells is more helpful for thermal runaway mitigation since the former can take advantage of total thermal mass of metallic inserts, while the latter only of the thermal mass of individual metallic inserts next to the damaged cell.

17. Key Words	18. Distribution Statement
lithium ion pouch cell, mitigation barriers, thermal mass, propagation, electric vehicle	Document is available to the public from the DOT, BTS, National Transportation Library, Repository & Open Science Access Portal, rosap.ntl.bts.gov.

19. Security Classif. (of this report)	20. Security Classif. (of this page)	21. No. of Pages	22. Price
Unclassified	Unclassified	52	

Form DOT F 1700.7 (8-72) Reproduction of completed page authorized

Table of Contents

List of Figures

List of Tables

Acronyms and Definitions

EC	electrochemical
ECT	electrochemical-thermal
MSMD	multi-scale multi-domain
NTGK	The Newman, Tiedemann, Gu, and Kim model
SOC	state-of-charge

1. Introduction

Studies on the safety of lithium ion batteries (LIB) have long focused on the impact and aftermath of the field failure of a single cell. This has been driven by the fact that LIB have traditionally been used for small devices where (1) failure of a single cell would have little impact beyond the device and its user, and (2) the battery is unlikely to see a truly abusive condition under normal use. As LIB are considered for larger systems, including vehicle electrification and electric grid applications, the impact of the failure of single cells and small groups of cells must be reexamined. Recent incidents have seen thermal events that have eventually consumed entire battery systems, stemming from myriad initial causes, including mechanical intrusion (Musk, 2013), overheating (Voelcker, 2012), and overvoltage/overcharging (Lowy, 2013). Not only are the causes of failure becoming more diverse, but the impact of these failures is increasing as well. Mitigation of thermal runaway in lithium ion cells and modules is still a challenge to be overcome for the wide-spread adoption of electric vehicles (Musk, 2013; Voelcker, 2012; Lowy, 2013; Arbizzani et al., 2011; Bandhauer et al., 2011; Campion et al., 2005; Dahn et al., 2011). Failure in a cell can trigger exothermal reactions, which increases the cell temperature (400-700 °C) (Lowy, 2013; Doughty et al., 2002, 2005, Ren et al., 2014; Jeevarajan et al., 1999) dramatically within ~ 10 sec (Jhu et al., 2011; Kim et al., 2007). If this excessive heat is not properly removed, adjacent cells or modules heat up. Furthermore, if the temperature reaches the onset of thermal runaway, it can result in cascading failure of the entire battery system.

The thermal runaway behavior of single lithium ion cells is well studied (Arbizzani et al., 2011; Bandhauer et al., 2011; Campion et al., 2005; Dahn et al., 2011; Doughty et al., 2002, 2005, Ren et al., 2014; Jeevarajan et al., 1999; Jhu et al., 2011; Kim et al., 2007; Roth, 2019; Crafts et al., 2004; Spotnitz et al., 2007). Typical responses include venting of battery gasses, ejection of cell contents, extreme temperatures and in some cases, self-ignition of the cell or ejected battery materials. What is less well known is how these behaviors may impact a larger, more complex system. The failure of a single cell taken on its own may have little impact on an electric vehicle system; however, the thermal and electrical impact on other cells in the system may be sufficient to cause a cascading runaway effect. In this scenario, the energetic thermal runaway of a single cell provides enough heat to neighboring cells. These cells then provide enough heat to chain the failure to their neighbors, continuing until the entire battery pack has been consumed. This worst-case scenario would result in a catastrophic release of energy within the confines of an electric vehicle causing significant damage and presenting a potentially dangerous situation for the operator. This possibility of propagation through a pack was modeled by Spotnitz et al. (2007). This work proposed that the likelihood of full battery pack failure was influenced by several factors, including the abuse response of the individual cells and the overall insulation of the pack. Particularly important, though, is the thermal contact to other cells since they predicted that cells directly neighboring cells were more likely to cause a propagation through a battery pack.

The electrical configuration of cells may impact how failure propagates. Offer et al. 2012) showed that even under normal conditions, varying resistances of connections between cells within a battery module might impact the local temperature of a cell. It is common practice to use blocking and discharge diodes within large parallel battery packs to prevent self-discharge of the battery through a shorted cell (Friel, 2019). However, the thermal separation between cells is often limited. Prismatic and pouch cells are often packed together either face to face or separated

by thin plates used for active cooling (Sun et al., 2012). Even if they are thermally separated, the electrical connections themselves have been shown to provide a path for heat transfer between cells (Kim et al., 2007).

Recent work exploring the behavior of battery systems has largely been focused on long-term performance issues (Offer et al., 2012; Sun et al., 2012; Kim et al., 2012; Lu et al., 2013; Troxler et al., 2014; Wu et al., 2004, 2013).; however, some information on failure propagation may be inferred. Much of the current handling of cell faults in battery packs involves the diagnosis and electrical handling of faulty cells within a system. Various methods exist to detect faulty cells Lu et al., 2013), and Kim et al. (2012) described a method for electrically isolating faulty cells from the battery pack. The science of fault detection is still in its infancy, and the most reliable indicators of battery health are still voltage and temperature monitoring of cells. Unfortunately, when considering battery safety, changes in cell voltage or temperature are only symptoms of a different issue and are not indicators of a root cause. These indicators often lag a root cause, and by the time a significant temperature increase or voltage change is observed, the cell is undergoing a thermal runaway event that is too late to arrest.

Several experimental (Finegan et al, 2018, 2019; Lamb et al., 2020; Torres-Castro et al., 2020) and numerical studies (Kim et al., 2007, 2012; Li et al., 2019; Shurtz et al., 2018a, 2018b; Kim et al., 2020; Mallarapu et al., 2020; Hatchard et al., 2001) are reported in the literature on safe battery design. In experiments, the physical behavior of battery packs under abuse conditions is observed using different damage initiation methods, such as pulsed laser, nail penetration, thermal ramp, and overcharge (Lamb et al., 2020), all of which increase the temperature of a trigger cell globally (thermal ramp, overcharge) or locally (nail penetration, pulse laser) up to the onset temperature of thermal runaway. For example, nail penetration can cause an internal short at a localized region, which heats up rapidly due to Joule heating and promotes exothermic decomposition reactions. On the other hand, in thermal ramp experiments, the temperature of a battery module increases at a much slower rate (5 °C/min in Lamb et al., 2020)) and hence the battery module is under quasi-thermal equilibrium conditions until it reaches the onset temperature for thermal runaway.

Thermal abuse reactions are modeled by Hatchard et al. (2001) and Kim et al. (2007). Hatchard et al. first suggested a lumped four-equation thermal abuse reaction model, which includes positive-solvent, negative-solvent, SEI decomposition and electrolyte decomposition reactions. Kim et al. then extended the model developed by Hatchard et al. in three-dimensions (3D) and studied multi-dimensional thermal runaway propagation behavior. Recently, Li et al. (2019) adopted a multi-scale multi-domain approach to model the Joule heat and electrochemical heat during nail penetration that initiates thermal abuse reactions, and consequently incorporated the four-equation thermal abuse reaction model to study thermal behavior happening during cascading cell failure events within a battery module. The effects of passive thermal management, such as the role of adding metallic inserts and the role of thermal contact resistances, are discussed.

In addition to comparisons with existing thermal runaway and propagation data, modeling has provided useful insight for future test design. For example, intercell heat transfer strongly affects intercell failure propagation rates; this observation led to the investigation of thermal spacers between pouch cells. It was confirmed that reducing heat release during cell runaway helped prevent propagation to neighbors. However, thermal spacers/barriers also bring about a negative situation, thermally insulating a cell not only during runaway but also during *normal operation*,

leading to undesirable heat retention. Such heat retention can lead to premature cell aging and safety issues. Therefore, an ideal barrier is one that thermally conducts at normal temperatures to prevent overheating and thermally insulates at runaway temperatures. The development of such material in partnership with Dr. Bryan Boudouris at Purdue University is investigated.

Previous work has been performed at Sandia National Laboratories exploring how battery failure may propagate in small strings of cells (Lamb et al., 2015). This work showed the impact that electrical configuration may have but was limited to small fully parallel or fully series strings. There is a significant gap in the knowledge of how propagating failure behaves in larger formats and how best to perform testing in a way that generates relevant results. This work explores the behavior at a larger scale of propagation testing and ultimately aims to provide a better empirical basis for the propagation testing of full scale electric vehicle batteries.

1.1. Previous Work

Sandia National Laboratories has previously released details on failure propagation testing using nail penetration methods (Lamb et al., 2015; Orendorf et al., 2017). This was chosen due to the very low energy imparted to the pack needed to induce failure. However, this may not always be realistic for every testing organization or laboratory. Other test methods studied have included single cell overcharge, single cell thermal ramp, high intensity light, and laser based initiation. These all impart varying amounts of energy, as estimated in Table 1.

Table 1. Example of energies needed to initiate thermal runaway on a 3 Ah LCO pouch cell

Test	Energy Source	Conditions	Estimated Energy
20 Pulse laser	IR Laser	20 1.9 J pulses	38 J
Nail Penetration	Mechanical	20 mm penetration ~200 lb peak load	1.8 J
Undirected Light	Quartz Lamp	Exposure to light source through aperture	6000 J[1]
Thermal Ramp	Thermal	Heat to 200 °C	6300 J[2]
Overcharge	Electrical	1C to 200% SOC	43200 J[3]

An example of previous work performed at SNL is shown in Figure 1 and has explored failure propagation in small packs of cells. This work has predominantly focused on using nail penetration failure as the initiation method, as this has a low energy input into the cell and can typically reliably produce a thermal runaway event in these configurations. However, this leaves little information on how changes to the initiation method chosen when designing propagation experiments might impact the behavior.

[1] Based on radiometer measured flux through aperture.
[2] Calculated for hypothetical 40g cell – larger cells will require more energy.
[3] Calculated for a hypothetical overcharge at 3 A and 4 V on a 3 Ah cell.

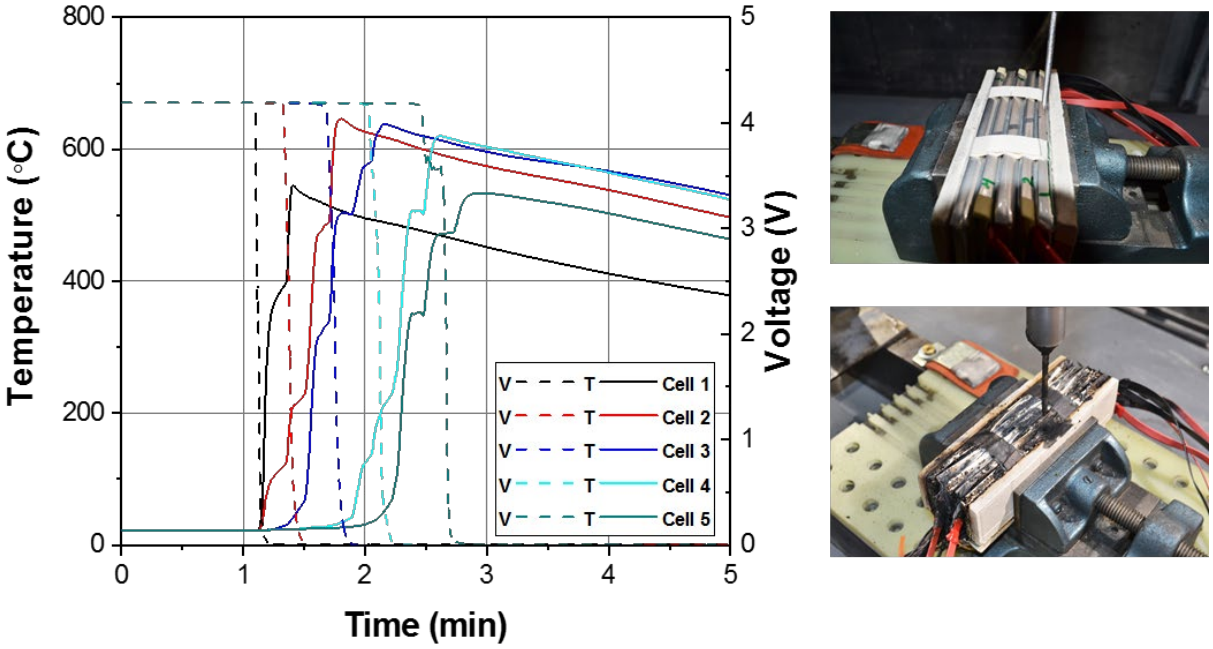

Figure 1. Failure propagation on 5-cell pack of $LiCoO_2$-graphite cells initiated through single-cell nail penetration

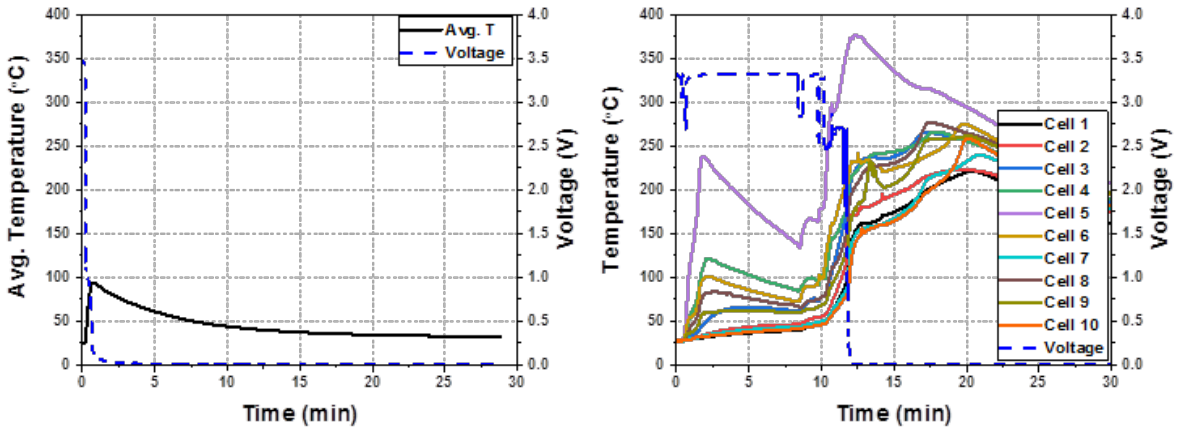

Figure 2. The nail initiated runaway of a single 26650 $LiFePO_4$ – graphite cell (left) compared to the propagating failure of a single cell failure within a 10-cell parallel string (right). In this case, a relatively benign single failure became significantly more severe when the failure occurred within a 10-cell string.

More recent work at Sandia has explored passive propagation mitigation strategies. This looks at the impact of simple metallic inserts as a means of mitigating heat transfer between cells during a thermal runaway event. For these tests, 5-cell strings were constructed using pouch type cells with varying thicknesses of both aluminum and copper plates between each cell. The general format of this test article is shown in Figure 2. A nail penetration test was used as the failure initiation technique, and plate thicknesses of 1/32" to 1/8" were used.

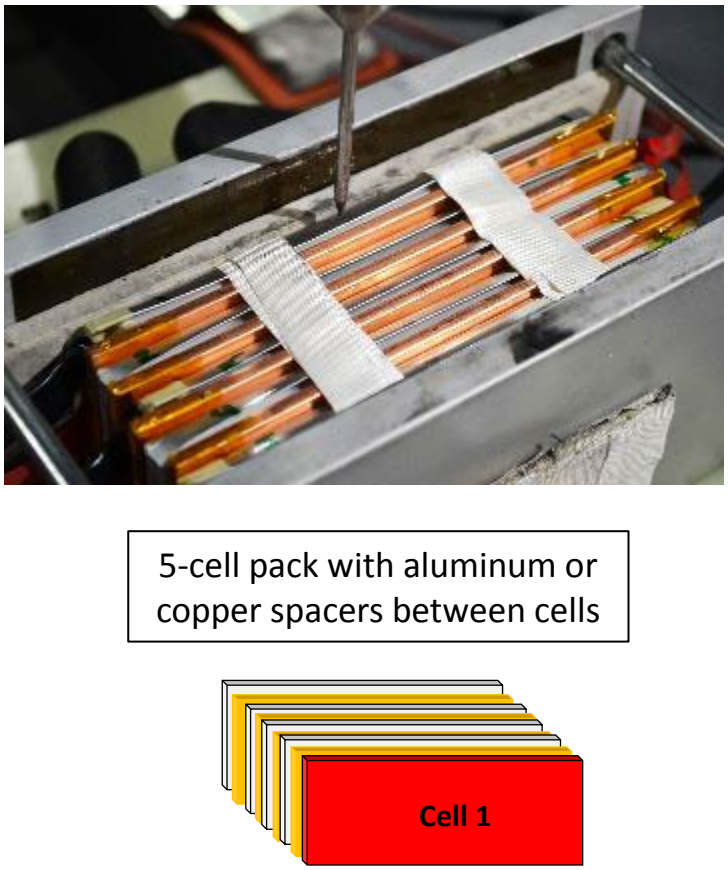

Figure 3. General schematic of pack construction for propagation

This technique effectively mitigated the propagating failure when using separation thicknesses of 1/8” and 1/16” as seen in Figure 3. Using a plate thickness of 1/8” shows that propagating failure was completely limited in that case. When using 1/16” plates, the nearest neighbor to the failed cell was observed to vent and lose voltage, but the propagating failure ended at that point.

When dropping to a thickness of 1/32”, complete failure propagating of the pack was observed, however, the time over which the failure occurred was increased, and the local temperature maxima can be observed as individual cells go into thermal runaway. This data is presented in Figure 4.

While this strategy has shown to be effective in small packs, it would constitute a significant increase in weight, cost, and volume if applied to a pack of hundreds of cells. However, it shows the potential of passive techniques to better understand how to mitigate battery failure propagation. Mitigation strategies building on this may use more sparsely interspersed plates to create propagation break points within a pack. However, it is difficult to explore every conceivable configuration and pack design experimentally, so a deeper understanding of the heat transfer and failure mechanisms that influence propagation is required. Well-validated models and targeted testing present the most reasonable path for a better understanding of these mitigation strategies. Recently, Sandia has taken advantage of internal multi-physics finite-element-based computational software to support battery safety studies. These software tools were developed to address safety aspects of nuclear weapons design, including primary battery

design, material thermal runaway, and fire environments. We have developed thermochemical heat source models and applied these to studying ignition criteria and cell-to-cell propagation. These models do require modest cell-chemistry-specific parameter fitting for each new system design.

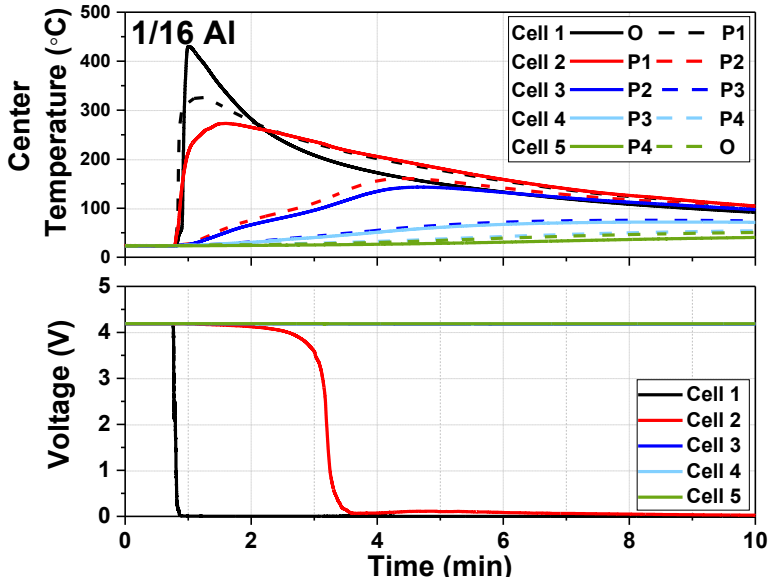

Figure 4. Data illustrating the impact of aluminum plates as a passive failure propagation barrier

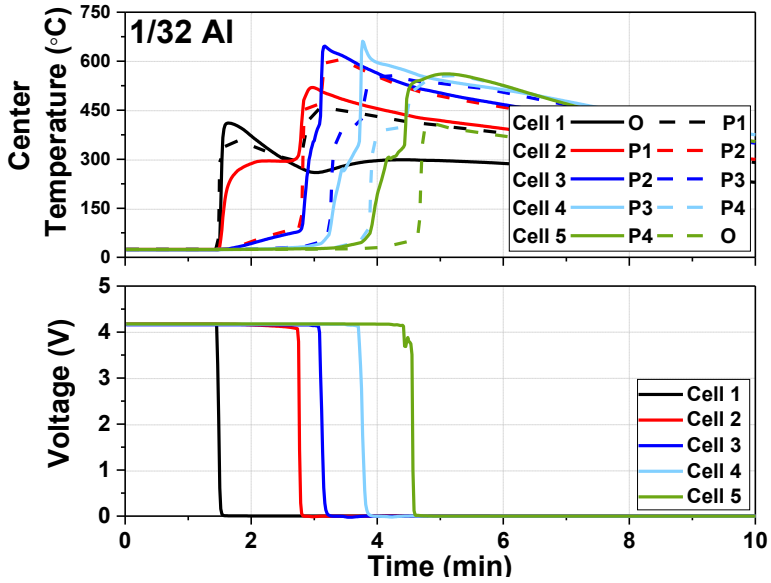

Figure 5. Data showing full propagation when using 1/32" aluminum plates between cells. The failure in this case was extended to require ~5 minutes before all cells were consumed.

2. Experimental Methods

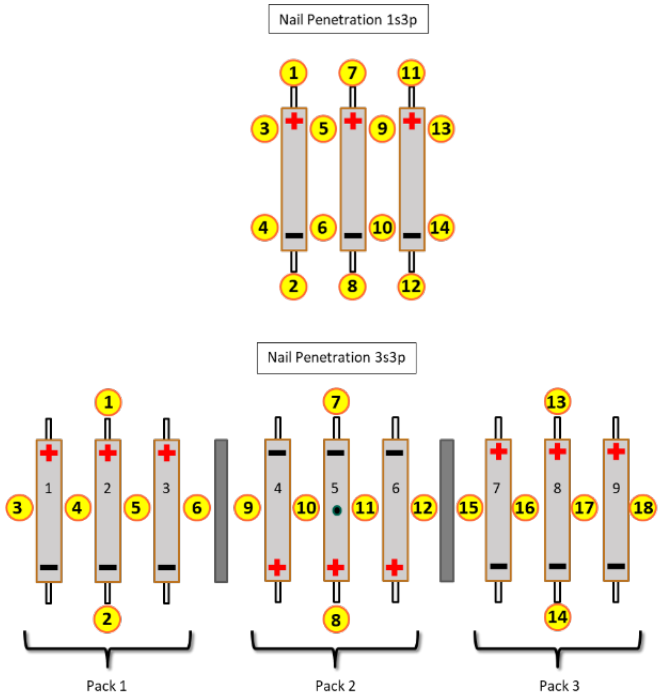

Figure 6. Experimental schematic of 1S3P and 3S3P modules

Propagation testing was based on tests of 5 Ah Kokam NMC cathode cells built into 1S3P individual modules, built into a 3S3P pack for performing module to module propagation tests. Figure 6 shows the general layout of the test modules along with numbered thermocouple locations. Initiation was performed on the central cell of the battery (Cell 5 in Figure 6). Monitoring during propagating failure included module and pack voltage, temperature monitoring at the numbered thermocouples, and visual recording of the failure as it progressed through the pack. Baseline testing was performed on single 1S3P modules and propagation mitigation was evaluated by placing plates at the indicated locations.

Initiation of the 1S3P modules was performed using both thermal and mechanical initiation. In the case of thermal initiation, the cell was heated at 5 °C per minute until failure to determine the baseline failure characteristic of a high temperature failure of the module. Nail penetration was used to establish an initial failure characteristic at near ambient conditions. For module to module nail penetration initiations were used on all tests.

3. Numerical Model

3.1. Quasi-1D model

A thermal runaway model was constructed in Sierra/Aria on a quasi-1D domain following the work of Kurzawski et al. (2020). Sierra/Aria is a multi-physics finite element package developed at Sandia National Laboratories (Notz et al., 2016). In this case, the heat equation is solved in the cells and inert materials, and the system of ODEs that describe the thermal source terms ($\dot{S}$) are solved at each element, neglecting transport of species between elements.

$$\frac{\partial(\rho c_p T)}{\partial t} = \nabla \bullet (k_\perp \nabla T) + \dot{S}$$

The heat equation is discretized in the direction perpendicular to the plane of the electrodes while the domain is lumped in the plane of the electrodes. The thermal conductivity in the plane of the electrodes ($k_\parallel$) is much greater than the thermal conductivity perpendicular to the electrodes ($k_\perp$) (Ahmad et al., 2018). The result is a quasi-1D formulation based on the lumped approximation that gains computational efficiency at the expense of spatial resolution.

Thermal properties for the cell, nail, copper spacers, and aluminum spacers are assumed constant and are listed in Table 2. Additionally, thermal contact resistances are specified at each solid interface: cell to cell, cell to spacer, and cell to end block. The thermal contact resistance is one of the primary factors in determining the gap crossing time for thermal runaway to propagate from one cell to the next. The cell to cell thermal contact resistance is taken as 0.004 m^2K/W while both the cell to spacer and cell to end block thermal contact resistances are 0.002 m^2K/W. A convective boundary condition is applied to all exterior surfaces with a convection coefficient of 10 $W/m^2/K$.

Table 2. Thermal properties of quasi-1D model

Materials	Density, ρ [kg/m^3]	Heat capacity, c_p [J/kg- °C]	Thermal conductivity, k [W/m- °C]
Cell	1,792.5	778	0.5 (cross-plane)
Copper	8,933	385	401
Aluminum	2,702	903	237
Nail (steel)	8,055	480	15.1

The thermal source term is comprised of three thermal runaway reactions and a short circuit heat source, the details of which can be found in (Shurtz et al., 2018a, 2018b; Kurzawski et al., 2020). Table 3 lists the relevant parameters for the short circuit reaction and three thermal runaway reactions: SEI decomposition, anode-electrolyte, and cathode-electrolyte. The SEI decomposition reaction is described by Richard and Dahn (Richard & Dahn, 1999) with a small modification according to our re-evaluation of the thermodynamics of the reaction (Shurtz et al., 2018a, 2018b). A novel anode-electrolyte reaction model is used that better accounts for the gradual heat release that typically occurs early in the thermal runaway process. This model also captures the rapid increase in the heat release rate that is also evident in calorimetry studies

usually above 200ºC. The heat release for these total reactions is determined by the overall thermodynamic change from the lithiated graphite and electrolyte to the observed products [30,40]. The cathode-electrolyte reaction was adapted from Hatchard (Hatchard et al., 2001) with recent updates to the net heat release based on thermodynamics from Shurtz (Shurtz & Hewson, 2020). We note that both the anode-electrolyte and cathode-electrolyte reactions depend on the state of charge (SOC) and the amount of electrolyte in the cell, which is estimated. The state of charge affects the amount of lithium in the anode and the degree of delithiation of the cathode, both of which affect the total possible heat release as discussed in (Shurtz et al., 2018a, 2018b; Shurtz & Hewson, 2020. For SOC near 100 percent, the electrolyte is often insufficient to fully oxidize the anodic lithium so that there is a slight reduction in that heat release.

Table 3. Reaction model parameters

Reaction	A [1/s]	E [kJ/mol]	ΔH [kJ/mol]
Short Circuit	0.0167	N/A	-405.2
SEI Decomposition	1.67e15	135.0	-52.42
Anode-Electrolyte	2.1e13	135.0	-281.4
Cathode-Electrolyte	3.51e11	122.52	-169.6

The joule heating from the short circuit induced by the nail penetration modeled as a heat source that partitions energy between the nail and electrically connected cells in the module where the nail penetration occurred. The reaction is modeled as

$$LiC_6 + MO_2 \rightarrow LiMO_2 + C_6$$

where lithium transfers from the anode to the cathode as the electrical energy flows through the short and releases energy in the form of Joule heating. The heating rate is given by

$$r_{short} = c_{C_6,total} A_{short} (X_{SOC})^{0.1}$$

where A_{short} is the inverse time scale that is inversely proportional to the total short circuit resistance, and X_{SOC} is the fractional state of charge given by $\min(c_{LiC_6}, c_{MO_2}) / c_{C_6,total}$.

This heat generated by the short circuit is portioned between the electrically connected cells and the nail. As the domain is lumped in the plane of the electrodes, the nail is not spatially resolved and is represented by a plane of material. Therefore, the volumes and resistances of the nail and cells cannot be used to partition the energy and a tuning parameter is introduced that describes the fraction of energy released in the nail. The effects of the short circuit parameters will be discussed in relation to experimental validation in the following section.

Initial exploration of extending reaction models from literature to module-scale simulations found that the speed of propagation was greatly over-predicted. These reaction models are generally calibrated on calorimetry data and are successful at capturing onset of thermal runaway and energy release but contain less information on reaction rates at higher temperatures found in cell-to-cell propagation scenarios. Kurzawski et al. (2020) proposed a mechanism for limiting the high temperature reaction rates with the diffusion rate of reactants from a characteristic particle in the electrodes. As each finite element in the numerical formulation contains some amount of

cathode, anode, separator, electrolyte, and inert materials, this model for intra particle diffusion serves to capture the effects of species transport on the reaction rate at a sub-element scale.

Matching serial reactions at the surface of a particle, the corrected reaction rate is given as $k/(1+Da)$ where the Damkohler number for electrode j is defined as follows.

$$Da_j = \frac{A_j\, exp\left(-E_j/RT\right)(r_o - r_i)}{a_p \rho D_{o,j}\, exp\left(-E_{D,j}/RT\right)} \frac{r_o}{r_i}$$

This non-dimensional number represents the ratio of the thermal runaway reaction rate to the diffusion rate of a reacting species through a spherical shell. Parameters for the diffusion coefficient expression are drawn from Guo et al. (2011) while the characteristic particle inner and outer radii, r_i and r_o, are estimated by matching the speed of the thermal runaway front moving through a cell.

3.2. Thermal-electrochemical model

The current thermal-electrochemical model is based on the MSMD model framework, which solves two equations for potential in the positive (Φ_+) and negative electrodes (Φ-) and one energy equation for temperature (T). [29,44]

$$0 = \nabla \bullet \left(\sigma_+ \nabla \phi_+\right) + j_{EC} + j_{short} \tag{1}$$

$$0 = \nabla \bullet \left(\sigma_- \nabla \phi_-\right) - j_{EC} - j_{short} \tag{2}$$

$$\frac{\partial\left(\rho c_p T\right)}{\partial t} = \nabla \bullet \left(k_{eff} \nabla T\right) + \dot{S}_{EC} + \dot{S}_{AB} + \dot{S}_{short} \tag{3}$$

The detailed description of all physical properties, constitutional relationships and source terms are listed in Li et al. (2019) and Kim et al. (2007, 2011), and hence are not repeated here. Thermal properties and heat transport parameters used in the current simulations are shown in Table 1 and Table 2, respectively.

Table 4. Thermal properties of material

Materials	Density, ρ [kg/m^3]	Heat capacity, c_p [J/kg- °C]	Thermal conductivity, k [W/m- °C]	Remarks
Jellyroll	2235	908	0.8(cross-plane) 27(in-plane)	
Copper	8978	381	387.6	Used in negative tab and metallic inserts
Aluminum	2719	871	202.4	Used in positive tab and metallic inserts

Table 5. Heat transport properties for the baseline case

Descriptions	Values	Remarks
Convective heat transfer coefficient [W/m^2- °C]	20	Applied at the exteriors of jellyroll
Emissivity [-]	0.8	Applied at the exteriors of jellyroll
Area-specific thermal contact resistances [m^2 °C/kW]	2.70 (jellyroll-jellyroll) 2.70 (jellyroll-metallic inserts) 10.8 (jellyroll-side plates)	Applied at the interfaces of components

The current numerical model is validated against a wide set of experiments. All simulations are conducted for cells at 100 percent SOC. First, Figure 1 shows schematic descriptions of 1S3P and 3S3P modules considered in both experiments and simulations. Model parameters, such as thermal contact resistance between components and convective heat transfer coefficients, are tuned based on the comparison between simulation results and experimental results for the 1S3P module cases. Then, same model parameters are applied for the 3S3P cases. In experiments, two metal plates (metallic inserts) are inserted between modules in 3S3P cases; two different materials, aluminum and copper, are considered.

We use the NTGK (Tiedemann & Newman, 1979; Gu, 1983) model for electrochemical modeling of Kokam 5Ah cells. NTGK modeling parameters are fitted using polynomials based on a wide range of discharge curves for the Kokam cells reported by the manufacturer. The same type of cells were also selected for constructing the battery modules in experiments. Figure 2 shows the comparison between discharge curves reported from the manufacturer and those from the current NTGK model.

In particular, a four-equation thermal abuse reaction model developed by Hatchard et al. (2001), which was later extended by Kim et al. (2007) to three-dimensions, is considered. Generally, the rate of thermal abuse reactions (Eq. (4)) and reaction heat (Eq. (5)) for the four reactions are expressed as:

$$\frac{d\overline{c_i}}{dt} = -A_i\left(\overline{c_i}\right)^{m_i} \exp\left(\frac{-E_{a,i}}{RT}\right) = -\dot{S}_i \tag{4}$$

$$\dot{S}_{AB.i} = H_i W_i \dot{S}_i \tag{5}$$

where $\overline{c_i}$ is a normalized concentrations of reactive materials and *i* is an index for thermal abuse reactions. Detailed descriptions of all thermal abuse reaction parameters are found in Hatchard et al. (2001) and Kim et al. (2007), and the parameters used in the current simulations are listed in Table 3.

Table 6. Thermal abuse reaction parameters

Reaction	Heat of reaction	J/g	Specific contents	g/m3	Normalized concentration	
SEI decomposition	H_{SEI}	257	W_C	6.14E5	C_{SEI}	0.15
Negative-solvent	H_{NE}	1714	W_C	6.14E5	C_{neg}	0.75
Positive-solvent	H_{PE}	314	W_P	1.22E6	α	0.04
Electrolyte decomposition	H_{EL}	155	W_E	4.07E5	C_e	1

3.3. Cell Stack Propagation Modeling

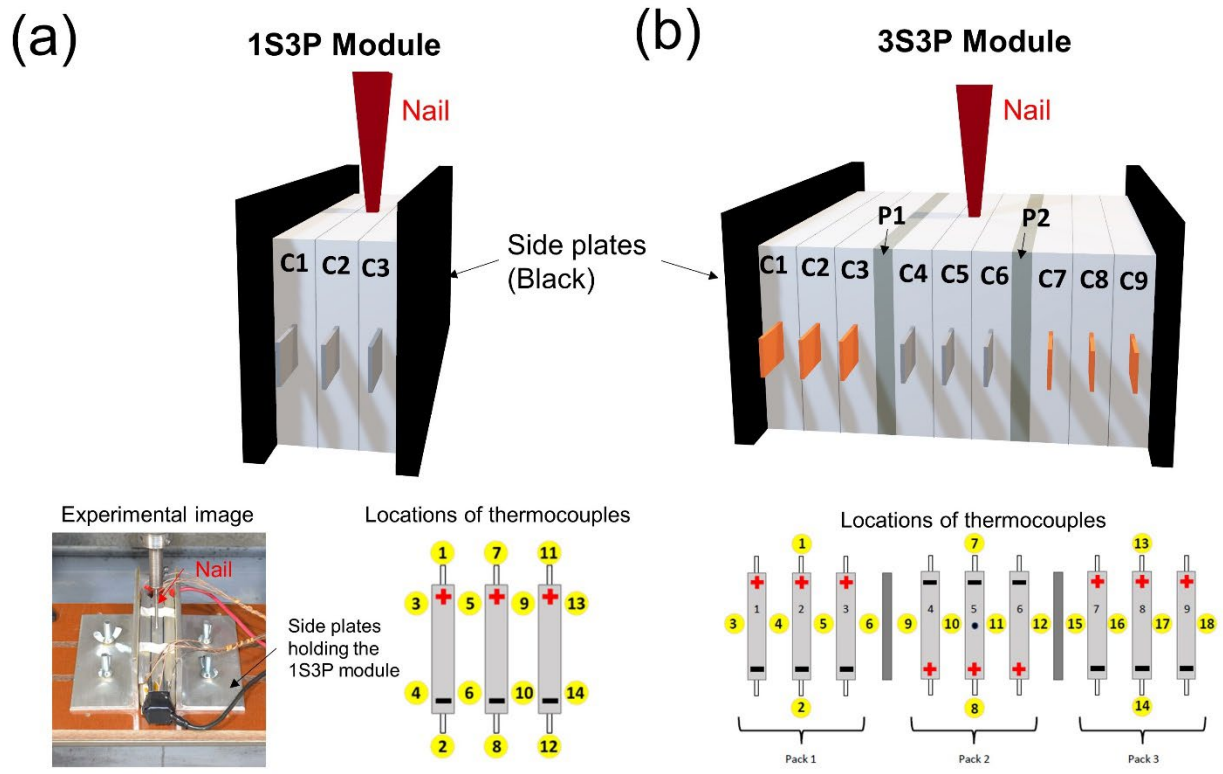

Figure 7. Schematic descriptions and locations of thermocouples for (a) 1S3P module and (b) 3S3P module

In the current simulations, we assume that the side plates holding the battery modules have infinite thermal mass since the side plates and the desk that holds the battery modules have much larger thermal mass than the battery modules as shown in Figure 7a and have very high thermal conductivity (~50Wm^{-1}K for steel). Hence, constant temperature for the side plates are assumed and the side plates are not explicitly modeled in the numerical simulations. For nail penetration simulations, we set the temperature of the side plates and the ambient temperature to be 25 °C (298K). The heating conditions for thermal ramp simulations are discussed in Section 3.4.

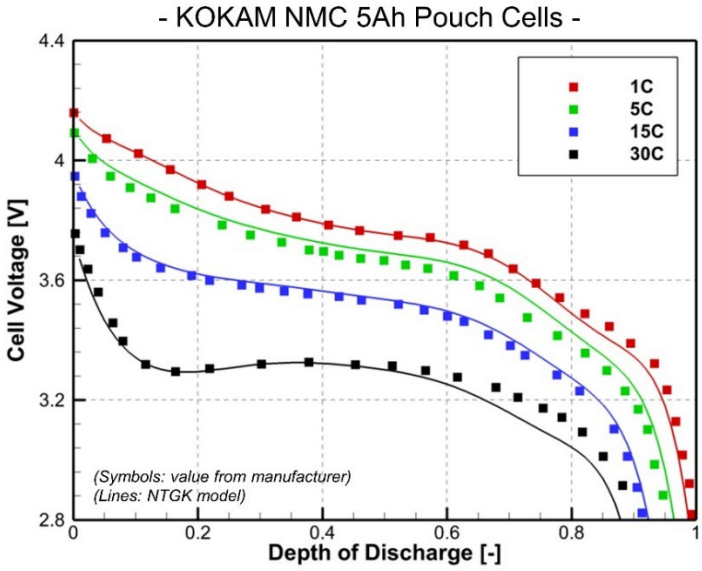

Figure 8. Comparison between the discharging curves reported by manufacturer (symbol) and the discharging curves modeled by NTGK electrochemical model (line)

The transport equations (Eq. (1-3)) are numerically discretized and solved by a commercial CFD software, Ansys Fluent version 19.2. Electrochemical and thermal source terms are implemented as user-defined-functions (UDF), and electrochemical and thermal abuse parameters are updated during iterations. In all simulations, residuals for positive, negative potentials and temperatures below 1e-8, 1e-8 and 1e-6 are achieved, respectively, which serve as a convergence criteria for the current numerical simulations. For nail penetration simulations, the ECT simulations start when the nail starts to penetrate the middle of the module in experiments. We assume that the nail penetration is complete before the onset of thermal events, and hence temporal mechanical deformations during nail penetration are not considered. The model triggers Joule heating at the location of nail penetration, by prescribing a volumetric short-circuit resistances of 2.5E-8 Ohm-m^3. The electrochemical (Eq. (6)) and thermal source terms (Eq. (7)) in the governing equations (Eq. (1-3)) are expressed as:

$$j_{short} = \frac{\phi_+ - \phi_-}{R_{sc}} \tag{6}$$

$$\dot{S}_{short} = \frac{\left(\phi_+ - \phi_-\right)^2}{R_{sc}} \tag{7}$$

4. Results and discussions

4.1. 1S3P Thermal runaway testing

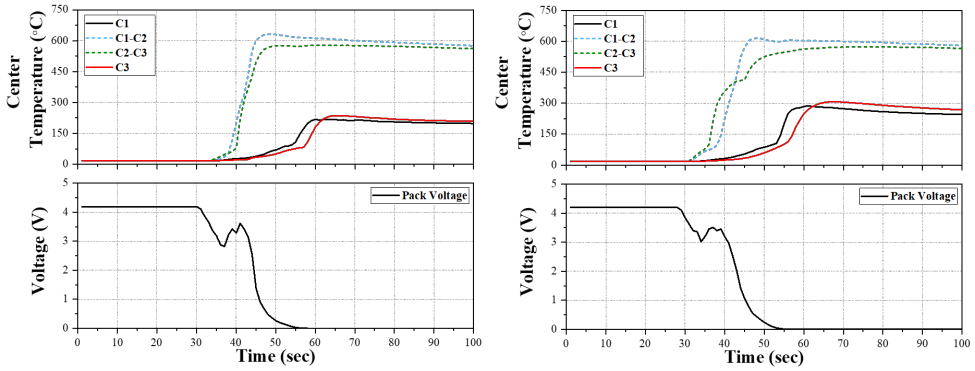

Figure 9. Results of nail penetration testing of 1S3P modules

Single cell nail penetration experiments are shown in Figure 9. This data gives a baseline of the thermal runaway behavior in a low energy injection scenario for initiating the thermal runaway process. This shows a peak observed temperature of just above 600 °C after cell failure and consumption of the entire pack within 30 seconds of the failure of the initial cell. The high temperature of the initial battery failure was able to quickly consume the module, and full voltage drop from the module was observed rapidly after the initial cell failure. The outer edges of the module reached a lower temperature of 200 to 300 °C with the peak temperatures of the outer edge being reached around the same time of full voltage loss from the pack. This gives the rough timing of the outer cell failures of this pack of ~30 seconds after the initial failure.

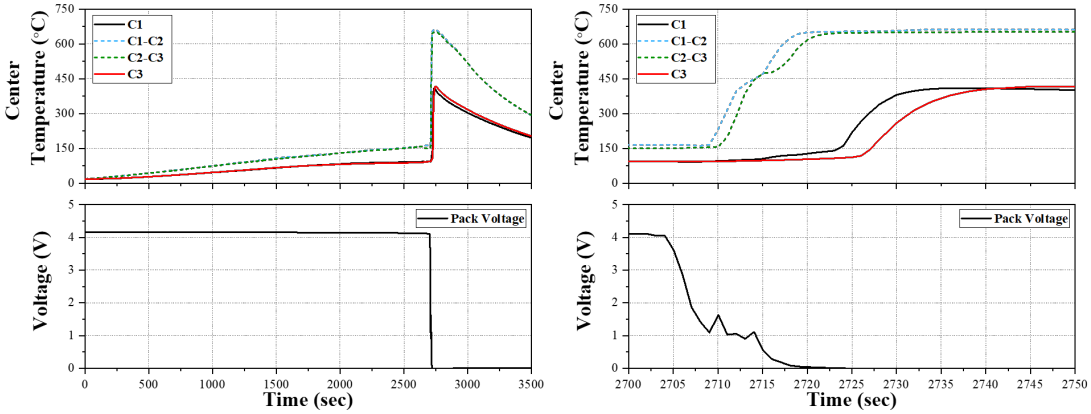

Figure 10. Results of thermal ramp testing of a 1S3P module

Thermal ramp initiation of the module is shown in Figure 10 that present the result when the baseline temperature of the entire module is increased by a heating cell. This shows the potential impacts of an elevated initial temperature, with thermal runaways occurring when all cells are showing surface temperatures of over 100 °C at the time of failure. This has an obvious impact on the peak temperatures observed, with peak temperatures reaching 650 to 700 °C, roughly 50

to 100 °C higher than those observed during nail penetration. The outer edge temperatures are also slightly elevated, with peak temperatures on the outside of the pack reaching ~400 °C, for a roughly 100 °C increase in observed peak temperatures. This had little impact on the observed propagation through the 1S3P module. The cells in this case fully propagated 20 to 30 seconds after the initial failure with voltage losses following the loss of the outer two cells in the module. These behaviors were reasonably close to the behaviors observed in nail penetration. The likeliest impact in more complex packs would be the increased temperature in the outside edges delivering more heat to neighboring modules.

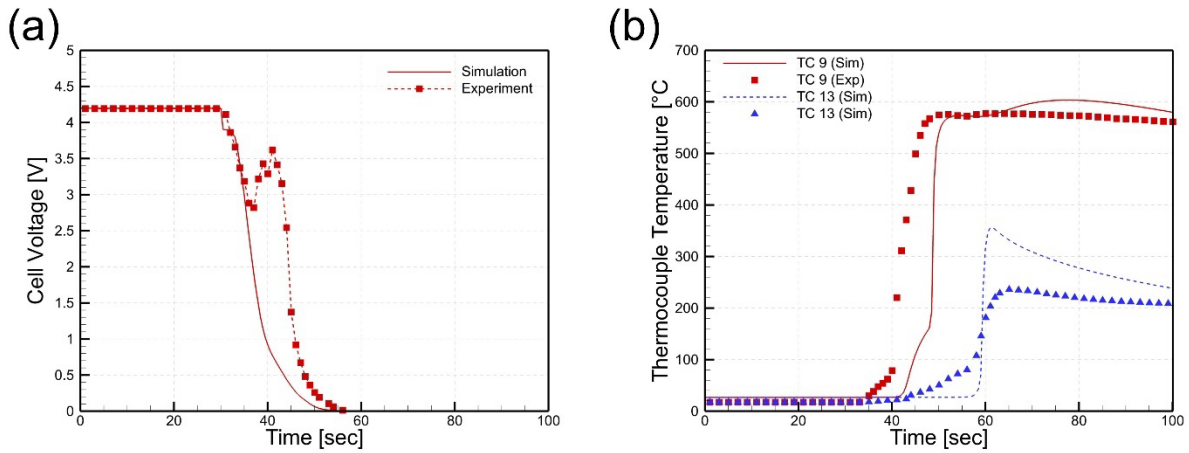

Figure 11. Comparison of (a) cell voltage and (b) thermocouple temperatures between experimentally measured data and simulations in the case of a 1S3P module

The following analysis of the nail penetration test compares the results of the above data to models developed at the National Renewable Energy Laboratory (NREL). Figure 11 first shows the comparison of voltage and temperature behavior measured by experiments and calculated using the current numerical model for a 1S3P module, which is designed to study the cell to cell damage propagation. Figure 11a shows the comparison in voltage behavior. In simulations, the voltage drops gradually right after the nail penetration starts, while the experiment shows fluctuating voltage after the nail penetration, which eventually drops to zero. It is worth noting that the simulation overpredicts the temperature of the outer edges of cell one and cell 3, which may impact propagation simulation.

The temperature trends between the numerical model and experiments agree well as shown in Figure 11b. The arrangement of thermocouple locations is shown in Figure 7a. It takes about 20 sec for thermal runaway to propagate from the middle of the module to the side plates along the thickness directions based on the difference in times between when the temperatures of thermocouples reach their maximum, which means that a characteristic time scale for cell-to-cell damage propagation is on the order of 10 sec for the current case.

4.2. 3S3P Failure Propagation Mitigation

Mitigation and behavior of module to module propagation were evaluated in 3S3P packs with results presented in this section. Mitigation barriers studied include copper and aluminum plates as well as G10 phenolic insulation. The thinnest barriers of 0.0625” are presented and compared in Figure 12 and Figure 13. The 0.0625 Al plates presented in Figure 12 show that the initial

failure reached maximum temperatures similar to those observed in the 1S3P studies above. The outer edge of the central pack sees notable temperature rise after ~30 seconds. Another 50 seconds after this point (80 seconds after the initial failure) signs of runaway are observed in the outer packs. Thirty seconds after this (110 seconds after initial failure) we see signs of complete failure of the battery pack.

This is compared to the same thickness of Cu plates shown in Figure 13. After initial failure, the outer cells of the central pack reach a temperature plateau after 25 seconds, a similar time scale to that observed in the above construction. Initial propagation to the outside modules is observed ~50 seconds later (75 seconds after initial failure). Complete failure of the pack is observed at 120 seconds after the initial failure. The low thickness of the plates used in these two tests, while showing some potential for a delayed thermal runaway, do not show significant differences between the two packs.

Further comparisons are made using 0.125" plates in Figure 14 and Figure 15. Figure 14 shows the results from 0.125" Al plates between modules and illustrates significant delays in full pack consumption when compared to the 0.0625" plates. A temperature plateau on the outside edge of the central module is observed ~25 seconds after the initial failure. This behavior is similar to that observed for the 0.0625" Al plates and is expected as there are no mitigating barriers within the module itself. The failure of the outer modules didn't initiate however until a ~115 seconds after the initial failure was observed, adding significant margin in the time to failure of this module. Full pack failure was not observed until ~165 seconds after the initial failure, adding nearly a full minute to the time required to consume the 3S3P pack. Peak temperatures meanwhile were similar to those observed for the 0.0625" barriers.

Figure 15 shows the results for module to module mitigation using 0.125" copper plates. This shows the outer edges of the target module reaching a temperature plateau after ~30 seconds, similar to other modules tested. Initial failure of the outer modules was observed after ~65 seconds. Full consumption of the pack occurred ~135 seconds after the initial cell failure. This showed a delay in the full propagation compared to the 0.0625" copper plates, but not as significant as that observed for the aluminum plates. This is likely an impact of increased thermal conductivity of copper which is explored in the thermal modeling on the following page.

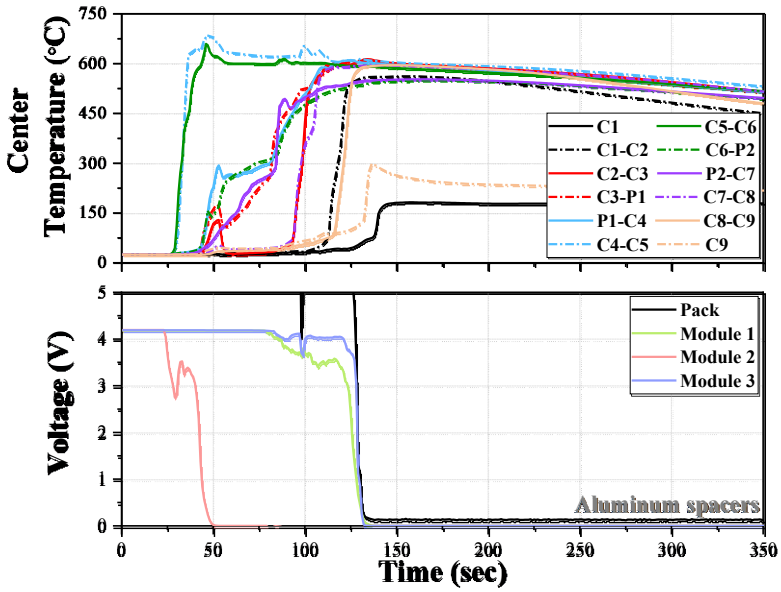

Figure 12. 0.0625" aluminum plates performed using nail penetration tests

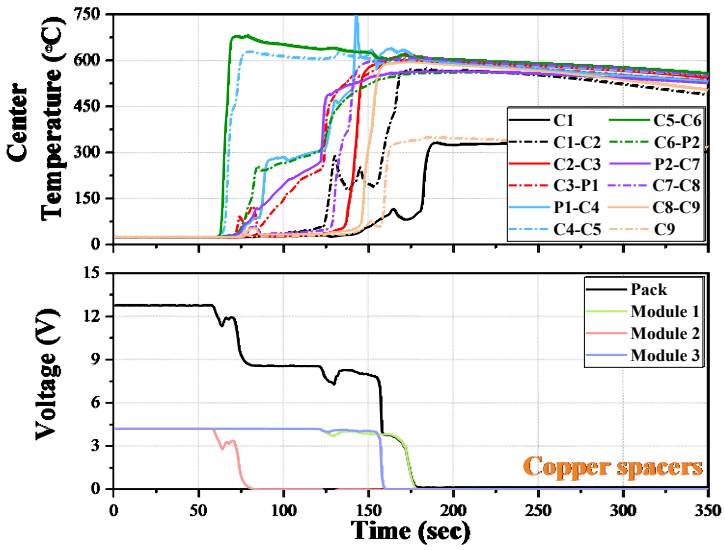

Figure 13. 0.0625" copper plates performed using nail penetration tests

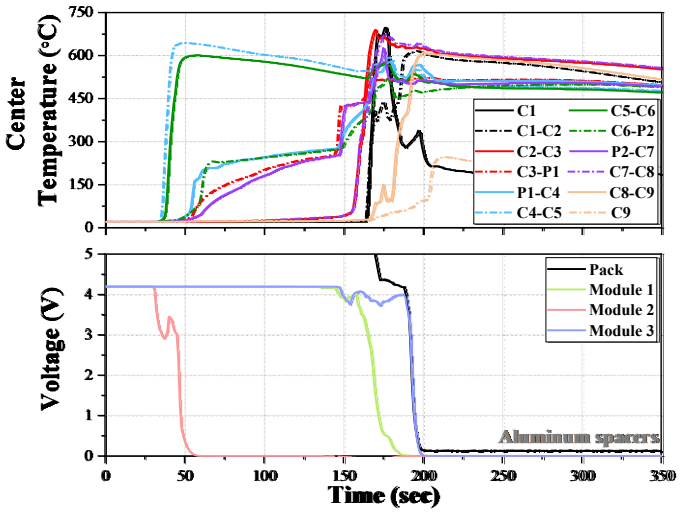

Figure 14. 0.125" aluminum plates performed using nail penetration tests

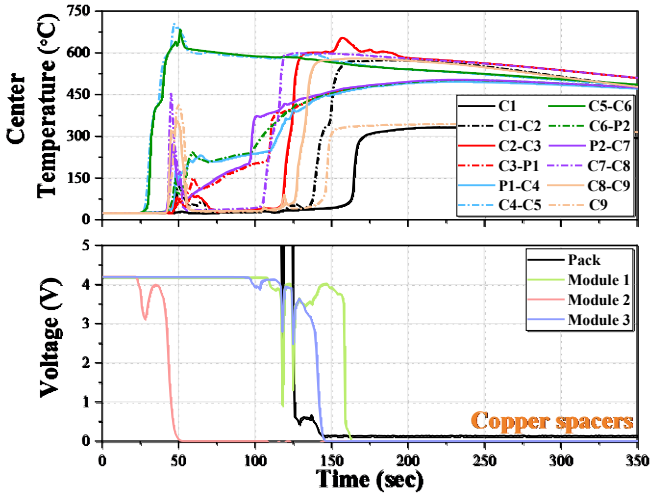

Figure 15. 0.125" copper plates performed using nail penetration tests

Comparisons are also made in case of 3S3P modules, in order to validate the numerical model in a more comprehensive manner, and to study the thermal behavior in module-to-module damage propagation. Two different materials for metallic inserts are considered; 0.125 inch Al plates, 0.125 inch Cu plates, where the Cu plates have approximately 40 percent more thermal mass than Al plates. As shown in Figure 16a (Al plates) and Figure 16c (Cu plates), the numerical model captures the experimental trends in terms of thermal runaway propagation intervals and maximum temperature rise.

The comparison of voltage trends shows that the current numerical model can predict the temporal behavior of cascading thermal runaway between modules, since the current model captures the time when module 1 starts to fail. In the case with Al plates Figure 16b), it takes ~75

sec for module 1 to fail after module 2 fails, while it takes ~ 95 sec in the case with Cu plates (Figure 16d). This is primarily due to the 40 percent larger thermal mass of Cu plates, compared to Al plates.

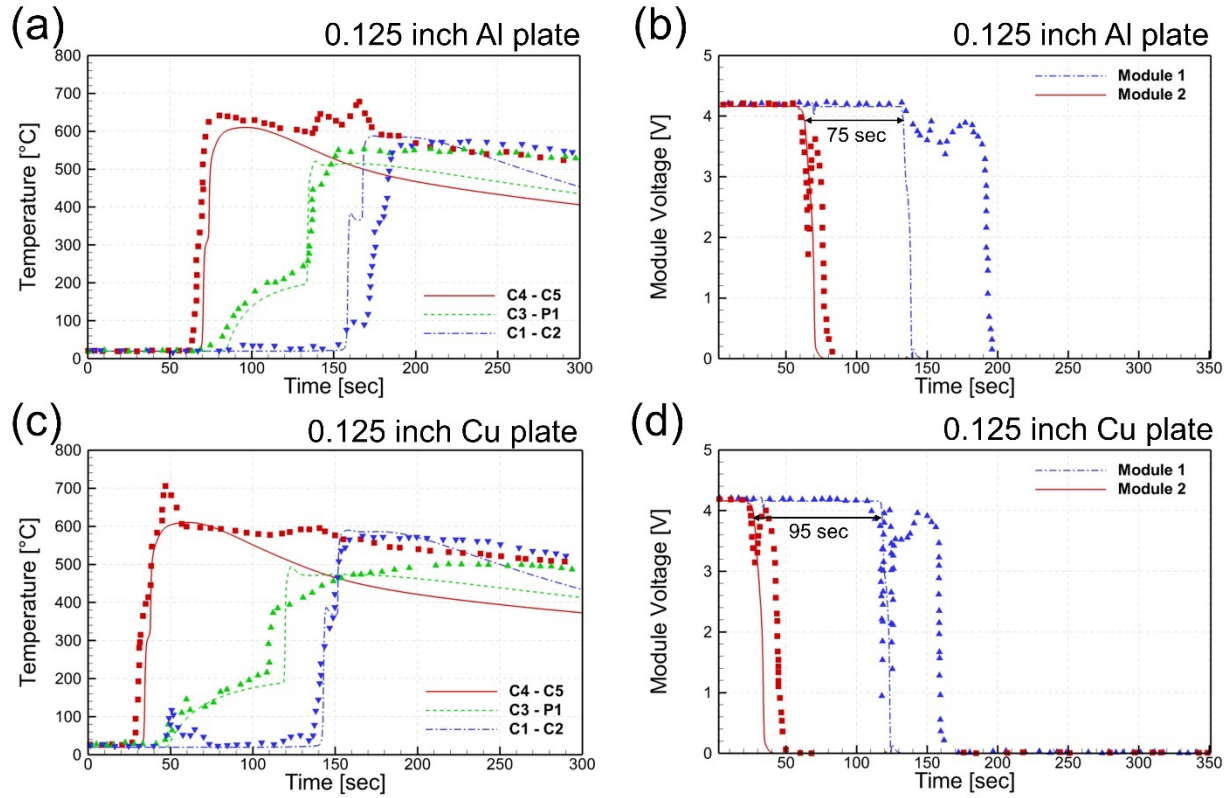

Figure 16. Comparisons of (a, c) voltages and (b, d) thermocouple temperatures between experimentally measured data and the simulated data in the case of 3S3P module (Fig. 4a-b: 0.125 inch aluminum plates, Fig. 4c-d: 0.125 inch cooper plate)

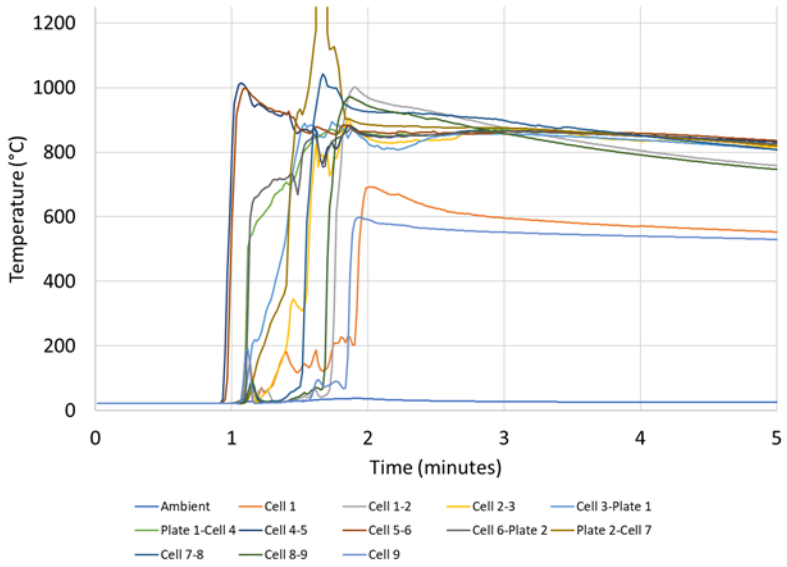

Figure 17. 0.0625" G10 phenolic insulation

Insulating barriers using G10 phenolic insulation were tested with results in Figure 17. A higher initial failure temperature is observed in these tests, potentially influenced by the insulating barriers. Propagation in this case begins to occur 30 seconds after the initial failure with the pack completely consumed approximately 60 seconds after the initial failure. Visual inspection showed partial damage to the phenolic barriers as well. This indicates that these barriers may be trapping heat within the modules leading to a somewhat more severe failure that rapidly propagates through the rest of the battery pack.

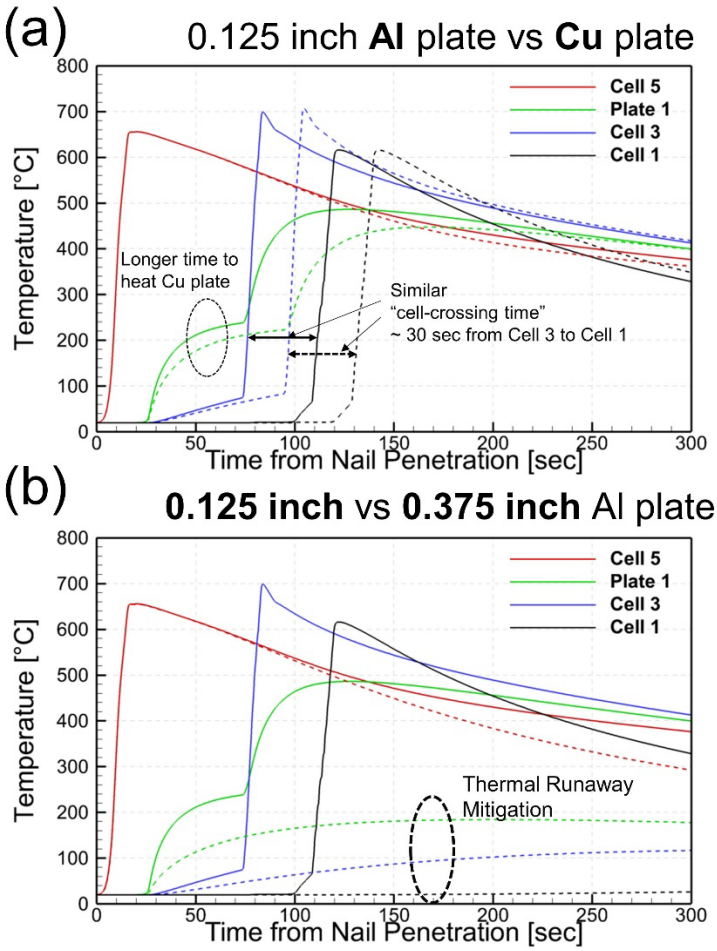

Figure 18. Comparisons of average temperatures of components (a) aluminum plates versus copper plates (b) 0.125 inch versus 0.375 inch aluminum plates

In order to further delve into the effect of thermal mass of metallic inserts, the average cell temperatures are plotted in Figure 18a. It is found that using Cu plates instead of Al plates results in longer time for the metallic inserts to be heated up, which results in delayed module-to-module damage propagation.

However, the "cell-crossing time" is similar for both cases (Al plates and Cu plates), considering that it takes ~ 30 sec for thermal runaway to propagate from cell 3 to cell 1 in module 1 for the both cases. (Cell-crossing time is defined as the difference between the times when the damaged cell and the adjacent cell reached their maximum average temperatures. Torres-Castro et al. (2020) used a similar definition in their work). This is primarily due to the fact that the metallic inserts are placed not between cells but between modules and hence do not play a significant role in cell-to-cell damage propagation.

In Figure 18b, temperature evolution for the case with 0.125 inch and 0.375 inch Al plates are compared, which also suggests that using larger thermal mass of metallic inserts is helpful for thermal runaway mitigation. Using thicker metallic inserts results in a slower rate of temperature increase for the inserts, and hence a slower rate of temperature increase for the adjacent modules as well, due to smaller temperature differences.

4.3. Quasi-1D validated results

The quasi-1D model was validated against five experimental configurations, where thermal runaway was initiated by nail penetration. The first configuration was 1S3P with metal end brackets on the sides of the stack (reference back to the experimental section), and the nail penetration occurred in the center cell (labeled C2). Four configurations of 3S3P modules with two spacer thickness and two materials were also used for the validation exercise. In each case, the three modules were separated by spacers of the following thicknesses and materials: 1/8" aluminum, 1/16" aluminum, 1/8" copper, and 1/16" copper. Thermal runaway was initiated in the center cell of the center module (labeled C5).

Preliminary results for one of the 1S3P nail penetration experiments are shown in Figure 19. We note that only two simulation temperature traces (dashed lines) are visible due to the symmetry of the system. For example, thermocouple C2-C3 overlaps with the thermocouple on the other side of cell 2, labeled C1-C2. The transition from joule heating to thermal runaway occurs slower in the simulations than in the model (around 20 seconds versus 10 seconds). The short circuit resistance is 25 mΩ and 20 percent of the energy from the short is partitioned to the nail. Additionally, while the magnitude of the initial peak temperature of the thermal runaway front encountering the end blocks is predicted well, the simulated end blocks appear not to be rejecting heat fast enough to keep up with heat transfer from the cells as they are cooling. This could be due to the geometry of the end blocks and their connection to the mounting surface which will not be investigated with this model.

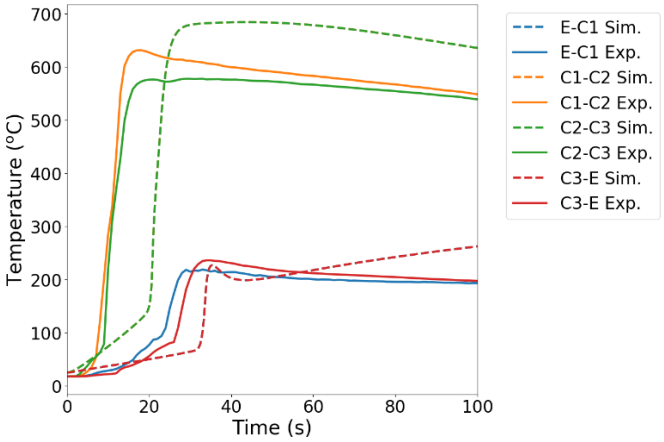

Figure 19. Preliminary predictions of propagation in a 1S3P case. Dashed lines represent simulations, and solid lines represent experiments

There is a substantial amount of uncertainty in the short circuit model parameters that govern the initiation of thermal runaway. Figure 20 shows simulation predictions versus two experimental replicates after several adjustments were made to the short circuit model. Here the short resistance has been lowered to 9 mΩ, the amount of energy partitioned to the nail has been increased from 20 percent to 40 percent, and the density of the planar nail has been decreased to match the true density ratio of the nail to the cell in the experiment. The density scaling is accomplished by multiplying the true nail density by the ratio of the nail volume to the planar nail volume. The planar nail density is 11.4 percent of the true nail density.

There is additional uncertainty in the initial amount of electrolyte in the cells as well as the amount of electrolyte that is vented when the pouch ruptures. In lieu of an electrolyte venting model, the mass fraction of electrolyte available for reactions in the simulation is reduced to approximate electrolyte loss due to venting. The initial mass fraction of electrolyte available for reaction is estimated at 0.0354 g electrolyte/g cell, while the electrolyte mass fraction in the cell where nail penetration occurs is further reduced by 40 percent to model greater mass loss due to the nail penetration. The final result of these adjustments (Figure 20) shows a good prediction of ignition time and over-prediction of the peak temperature in the center cell. The side cells tend toward a small underprediction of the peak temperature. It is likely that the parallel configuration short circuit transfers too much electrical energy to the center cell, suggesting that the cell degradation during short-circuit/runaway stops the parallel-circuit short-circuit process at some point. We have not attempted to correct for this phenomenon.

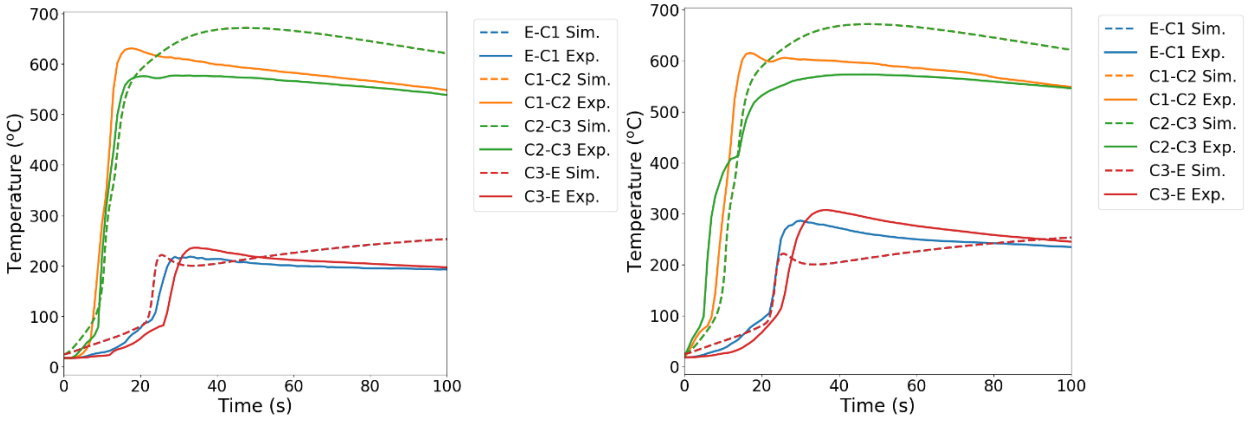

Figure 20. 1S3P simulation predictions versus experiments after short-circuit adjustment

Figure 21 and Figure 22 show the 3S3P temperature comparisons between experiments and simulations with a tuned short circuit. In general, the heat release and propagation speed across the side modules is predicted well in each case. The time delay for propagation across the spacers is predicted well in the 1/16" spacer cases, but there is more variance in the 1/8" spacer cases where predictions of thermal runaway initiation in the side modules occurs faster than experiments for the aluminum spacers and slower than the experiments for the copper spacers.

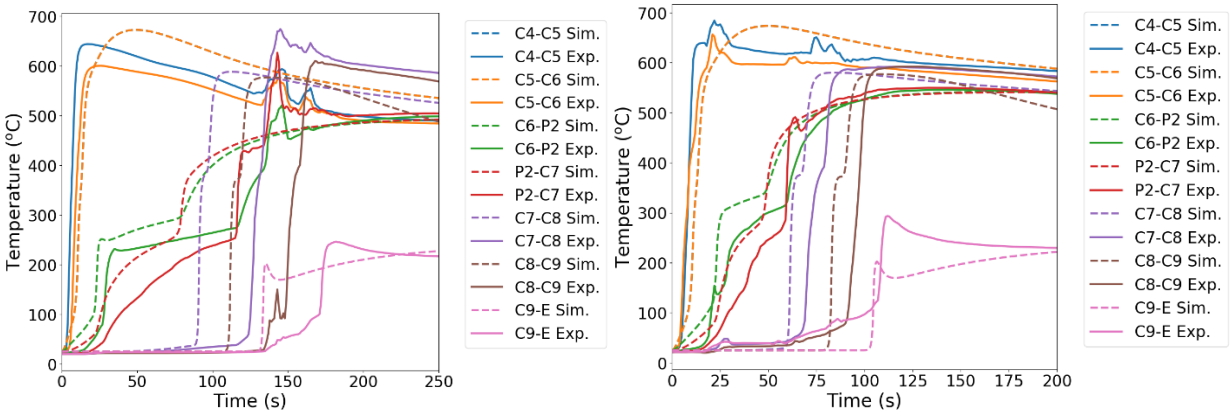

Figure 21. 3S3P with 1/8" (left) and 1/16" (right) aluminum spacers

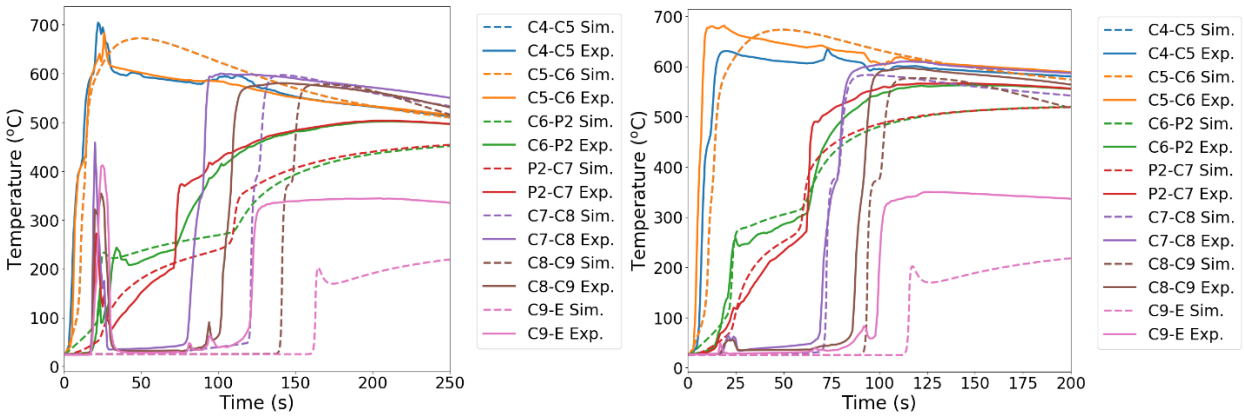

Figure 22. 3S3P with 1/8" (left) and 1/16" (right) copper spacers

The temperature at end block thermocouple (C9-E) is underpredicted in the copper spacer cases (see Figure 22) due to an extra layer of insulation material between the end cells and mounting brackets that was not included in the current model. In the 1S3P cases and 3S3P aluminum spacer cases, the end cells are directly touching the metal mounts resulting in greater heat transfer from the end cells.

4.4. Interplay among three parameters in passive thermal runaway management

As noted in the experimental and numerical studies in previous section, passive thermal runaway management is helpful for battery safety under abuse conditions. We identify that three parameters play critical roles in passive thermal runaway management.

- Thermal mass of metallic inserts
    - Metallic inserts absorb large amount of excessive heat generated during thermal abuse reactions.
- Thermal contact resistance:
    - Thermal contact resistance between components (cell-to-metal plates or cell-to-cell) causes a "gap effect", which delays heat transfer from the damaged cell to the adjacent cell (or metal plates). Hence, large "gap effect" results in more time for heat removal and reduces the maximum temperature at the interface.
- Heat removal rate:
    - Natural convection, radiations or forced convection (e.g., via cooling channels) removes heat generated during thermal abuse reactions and a higher rate of heat removal is favorable for battery safety.

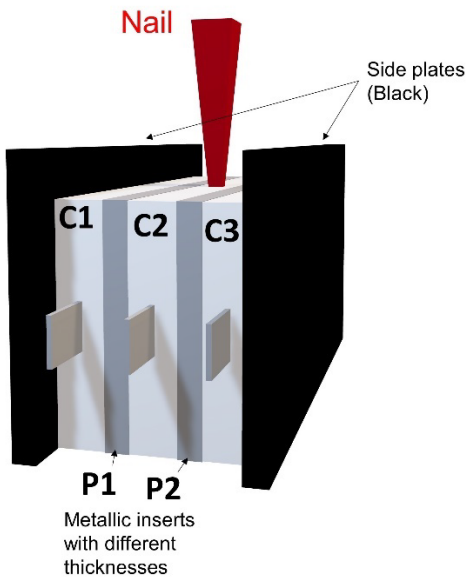

Figure 23. Schematic of a 1S3P module with two metallic inserts between the cells to study the role of three parameters associated with passive thermal management on thermal runaway mitigation

In order to numerically study the effect of those three parameters in detail, 1S3P modules with metallic inserts between cells are designed as shown schematically in Figure 23. Different sets of thickness values for the metallic inserts, material choices for metallic inserts, thermal contact resistances between cells and metal plates as well as heat transfer coefficients are considered in the simulations, while other conditions such as cell dimensions and electrochemical parameters remain same.

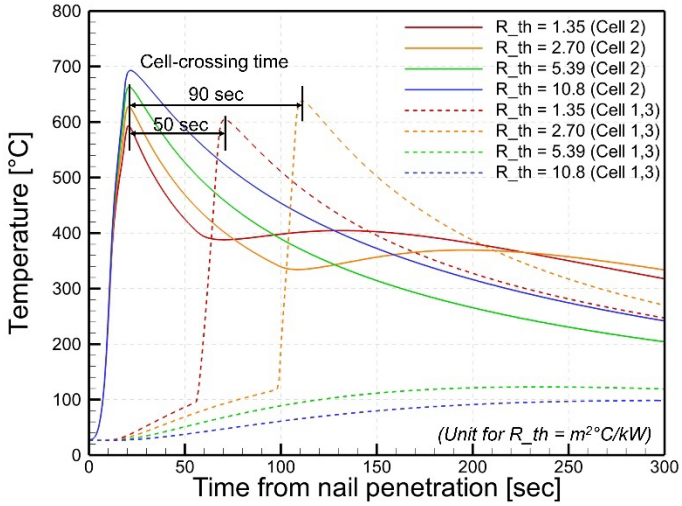

Figure 24. Comparison of average cell temperature behavior at different area-specific thermal contact resistances (thickness of aluminum plates = 0.125 inch)

Figure 24 compares the average cell temperatures at different thermal contact resistances to study the effect of spacing between cells on the thermal runaway mitigation. In the case of the lowest thermal contact resistance (1.35 m^2 °C/kW), thermal runaway mitigation is not achieved and the cell crossing time is 50 sec. By increasing the thermal contact resistance further, the cell-crossing time increases to 90 sec at 2.70 m^2 °C/kW and reaches sufficiently large values at R_{th} > 5.40 m^2 °C/kW, implying that thermal runaway mitigation is achieved. To sum up, higher thermal contact resistances result in progressively increasing cell-crossing time, and hence a larger fraction of the generated heat is removed.

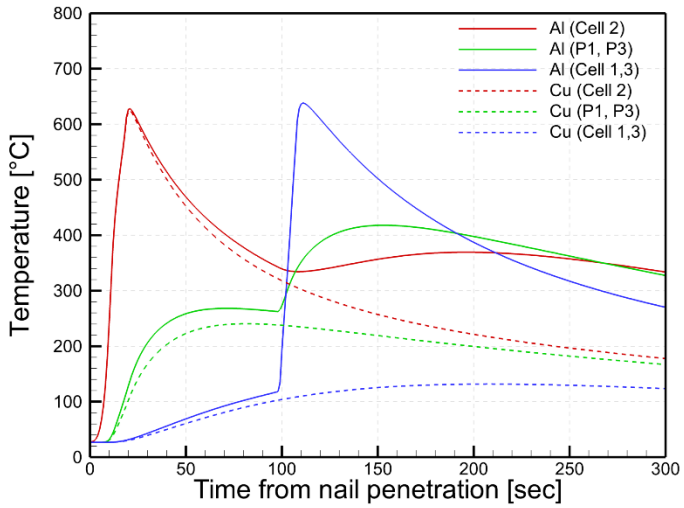

Figure 25. Comparison of average cell temperatures behavior between the case with aluminum plates and the case with copper plates (R_{th} = 2.70 m^2°C/kW, thickness of aluminum plates = 0.125 inch)

To understand the effect of thermal mass on the thermal runaway mitigation, we compare the average temperature across modules with different materials for metallic inserts. Similar to the results in the previous section (Fig. 4), using higher thermal mass for metallic inserts (Cu plates have 40 percent larger specific heat capacity compared to Al plates) results in slower temperature rise for the plates, and consequently slower temperature rise in the adjacent cells (cells 1 and 3).

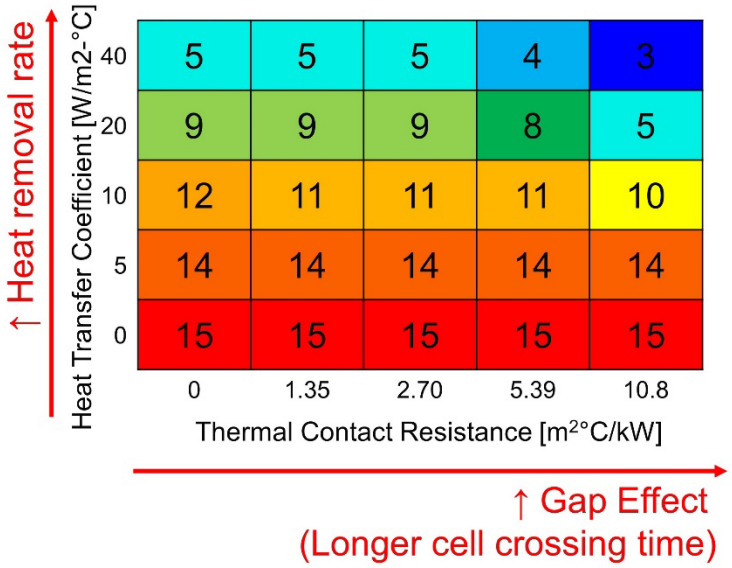

Figure 26. Minimum metal thicknesses for thermal runaway mitigation depending on area-specific thermal contact resistances and effective heat transfer coefficients. Aluminum metallic inserts are used for this example.

To study the effect of cooling rate as well as the interactions among the three parameters, a map of minimum metal thicknesses for thermal runaway mitigation is plotted in Figure 26. The minimum metal thickness is defined as the minimum thickness of metallic inserts that guarantees thermal runaway mitigation. In the current simulations, we consider a range of metallic inserts from 15 mm to 1 mm and the thickness of metallic inserts is decreased by 1 mm until the thermal runaway of adjacent cells (cell 1 and cell 3) sets in. If the temperatures of adjacent cells remain less than 200 °C for 10 min after the nail penetration in cell 2, we consider that thermal runaway is mitigated.

To consider the condition when there is no heat dissipation, we numerically turned off the radiation to surrounding and the heat dissipation to the side plates. For this case, heat dissipation is controlled only by varying convective the heat transfer coefficient at the exterior surfaces.

This map first suggests the importance of heat dissipation on thermal runaway mitigation. By increasing the convective heat transfer coefficients, the minimum metal thicknesses for thermal runaway mitigation are greatly reduced. At h=0W/m^2 °C and R_{th}=0m^2 °C/kW, 15 mm-thick metallic inserts are needed to ensure thermal runaway mitigation. However, at h=40W/m^2 °C and R_{th}=0m^2 °C/kW, we only need metallic inserts of one-third the thicknesses for thermal runaway mitigation.

Increasing thermal contact resistance helps thermal runaway mitigation as well, as seen in Figure 26 which shows the tendency of decreasing minimum metal thicknesses for thermal runaway mitigation with increasing thermal contact resistance. As discussed previously, increasing thermal contact resistances results in longer time for thermal runaway propagation, which results in more time for heat dissipation before thermal runaway at the adjacent cells is triggered. As a result, at h=0W/m^2 °C, increasing thermal contact resistance does not help thermal runaway mitigation as no heat is dissipated to surroundings and hence thermal runaway at the adjacent

cells are eventually triggered. To sum up, the "gap effect" is only meaningful when there is sufficient heat removal rate. Further reduction of temperatures would likely require some means of removing the heat in this case, such as forced air or liquid-cooling.

4.5. Effect of configurations of metallic inserts

In the last section we numerically studied the role of the three parameters of passive thermal management on thermal runaway mitigation. In this section, we consider two different configurations of placement of metallic inserts and study the effect of their configurations on thermal runaway mitigation.

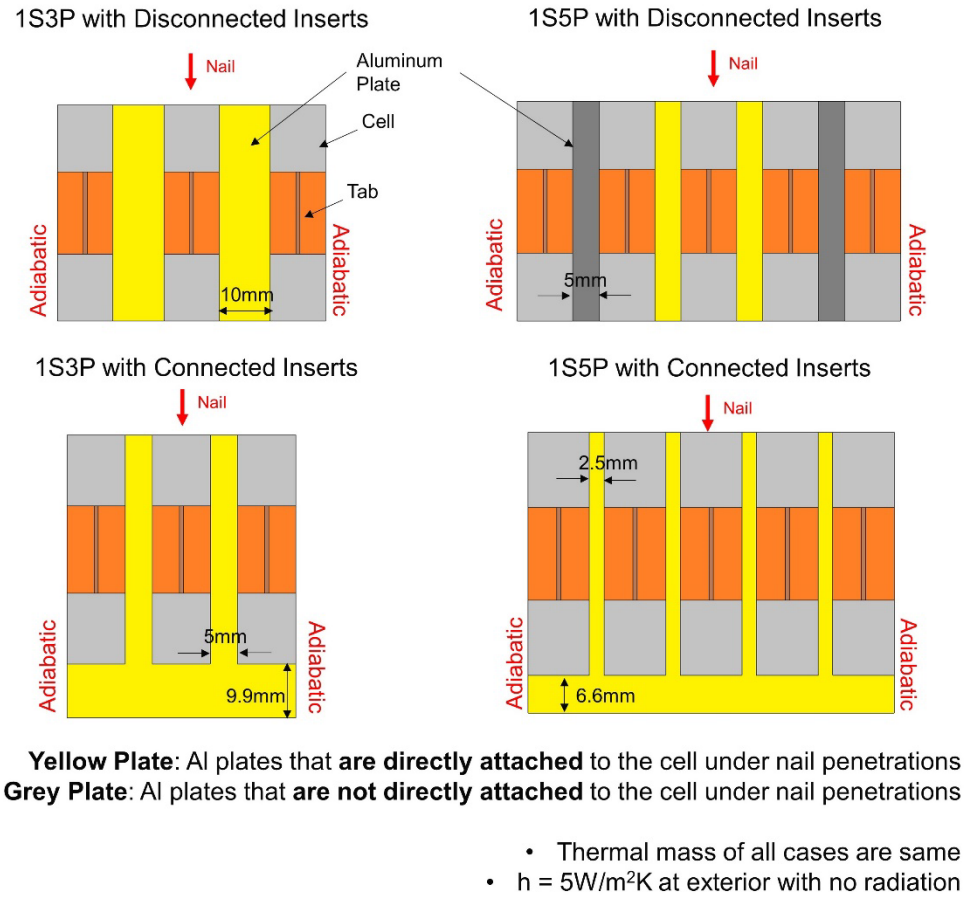

Figure 27. Schematics of the four configurations of battery modules considered to study the effect of configuration of metallic inserts on thermal runaway mitigation

Figure 27 shows configurations of metallic inserts and battery modules considered in the numerical model. The cases with "disconnected inserts" means that disconnected rectangular plates are placed between cells, while the cases with "connected inserts" means that rectangular plates are connected by being attached to the base plates and the cells are placed at the empty spaces. Then, the thermal behavior of the four different configurations of battery modules under nail penetration are studied. Note that the four configurations have the same thermal mass for metallic inserts.

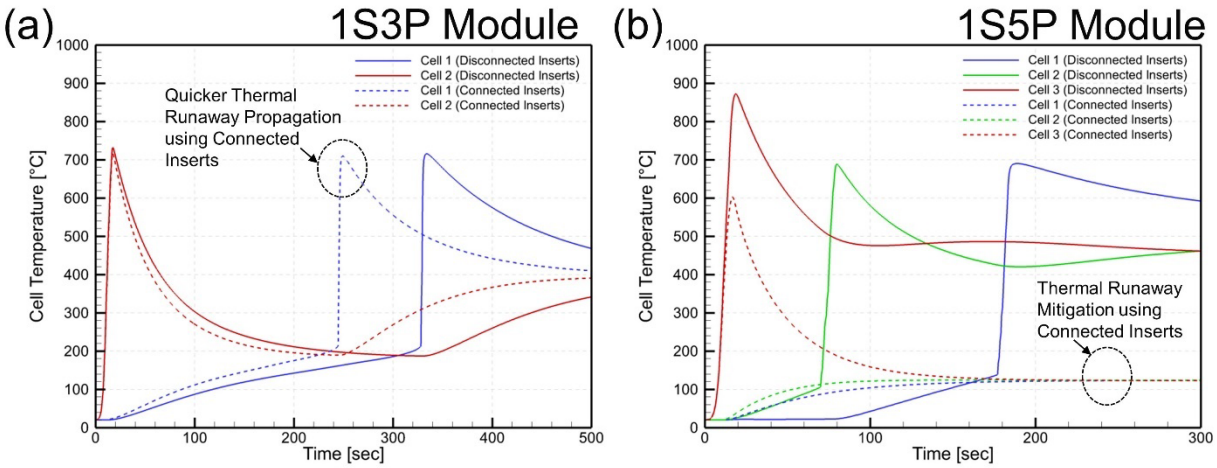

Figure 28. Comparison of average cell temperatures for the four different configurations of battery modules: (a) 1S3P with disconnected and connected metallic inserts (b) 1S5P with disconnected and connected metallic inserts

In case studies with 1S3P modules, using connected metallic inserts are not helpful for preventing thermal runaway propagation as seen in Figure 28a. The larger interfacial area between the metallic inserts and the jellyrolls promotes even faster heat transfer from the damaged cell (cell 2) to the adjacent cells (cell 1, 3) for this case, resulting in much shorter cell-crossing time compared to 1S3P case with disconnected inserts.

However, using connected metallic inserts is very helpful for thermal runaway mitigation in the case with the 1S5P module. As seen in Figure 28b, cascading propagation of thermal runaway is observed in the case with disconnected inserts, while thermal runaway is successfully mitigated for the case with the connected inserts.

The underlying reasons are:

- In the 1S3P module, connecting the metallic inserts does not increase the thermal mass of metallic inserts attached to the cell under nail penetration; and
- In the 1S5P module, accessible thermal mass of the metallic inserts attached to the cell under nail penetration are increased 100 percent by connecting the inserts.

Therefore, for battery pack safety, configuration of metallic inserts should be designed to maximize accessible thermal mass of metallic inserts attached to individual cells under abuse conditions.

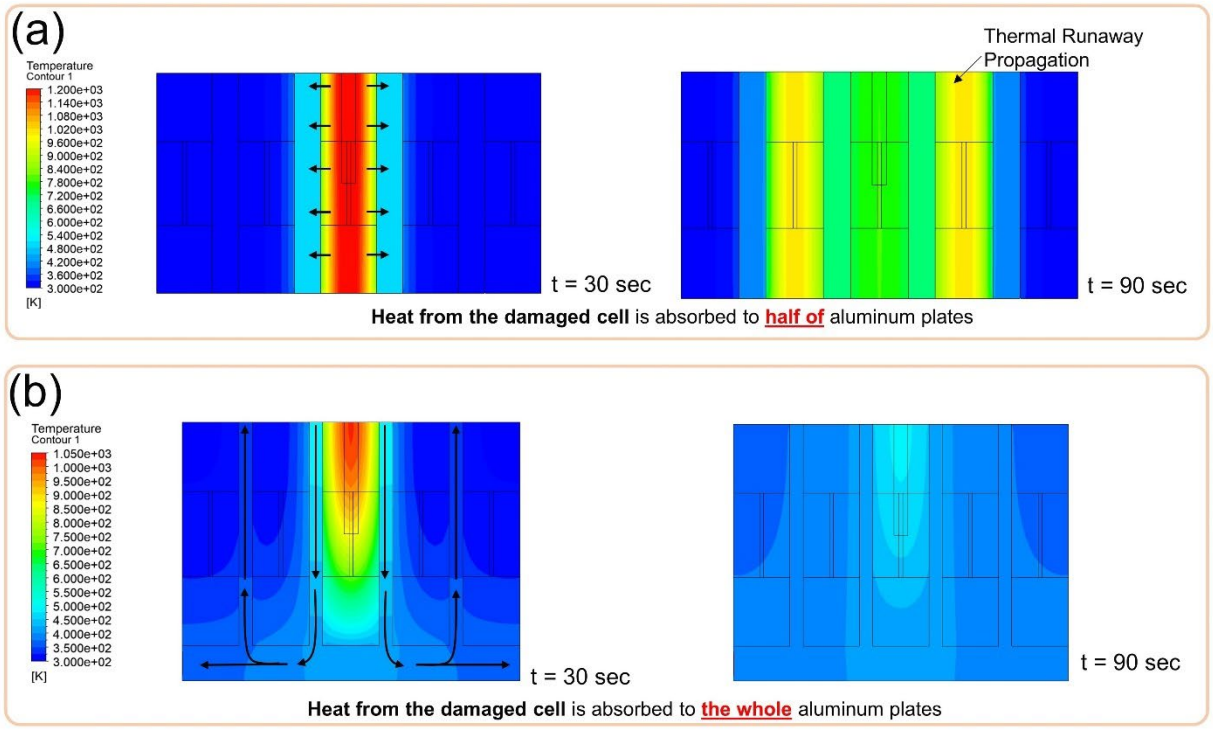

Figure 29. Temporal evolution of temperature at mid-sections (a) 1S5P with disconnected inserts (b) 1S5P with connected inserts

To illustrate this in more detail, comparisons of the temporal evolution of temperature at the mid-sections are made for the case with disconnected inserts and connected inserts. Figure 29a (1S5P with disconnected metallic inserts) shows that the excessive heat generated is only absorbed to the two adjacent metallic plates attached, and the direction of heat transport is mainly limited to through-thickness direction of the cell. At 90 sec, as the adjacent cells are sufficiently heated up to reach their onset temperature of thermal runaway.

However, the excessive heat generated is distributed to the whole network of metallic plates as shown in Figure 29b (1S5P with connected metallic inserts), and heat transfer takes place both in the longitudinal and transverse directions. Due to the much larger thermal mass of metallic plates attached to the damaged cell and larger surface area for heat dissipation, thermal runaway is successfully mitigated.

The engineering implications of this analysis is that adopting such similar concepts (connecting metallic inserts) are helpful under the conditions that the battery pack is partially damaged, such as in a vehicle crash. Furthermore, such design can be also helpful in terms of heat dissipation due to high thermal conductivity of base plates and hence excessive heat is more uniformly removed from the base plates through the heat sinks. The current numerical model can be extended to design more practical battery packs with cooling channels and heat sinks by incorporating flow models.

4.6. Thermal ramp simulations

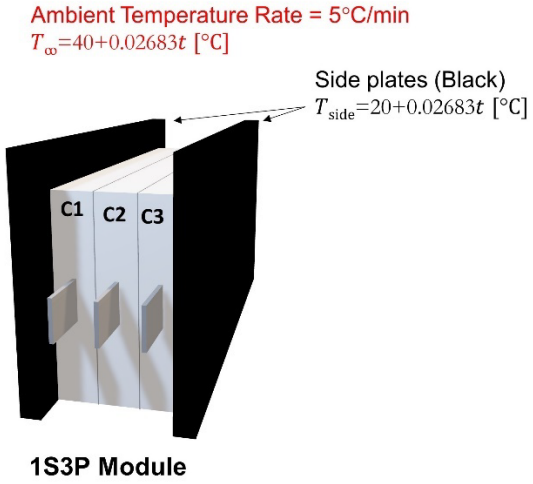

Figure 30. Schematic of a 1S3P module used for thermal ramp experiments and simulations

Figure 30 shows the schematic of the simulation conditions for thermal ramp simulations. The ambient temperature is initially set to 40 °C, in order to promote heat transfer between cells and ambient, are assumed to increase at the constant rate of 5 °C/min. However, the temperature at the side plate is initially at 20 °C and increases at a constant rate of 5 °C/min. All other parts including tabs and jellyrolls also have an initial temperature of 20 °C and their temperature increases due to convective and radiative heat transfer from the ambient. Properties regarding heat transfer are listed in Table 3.

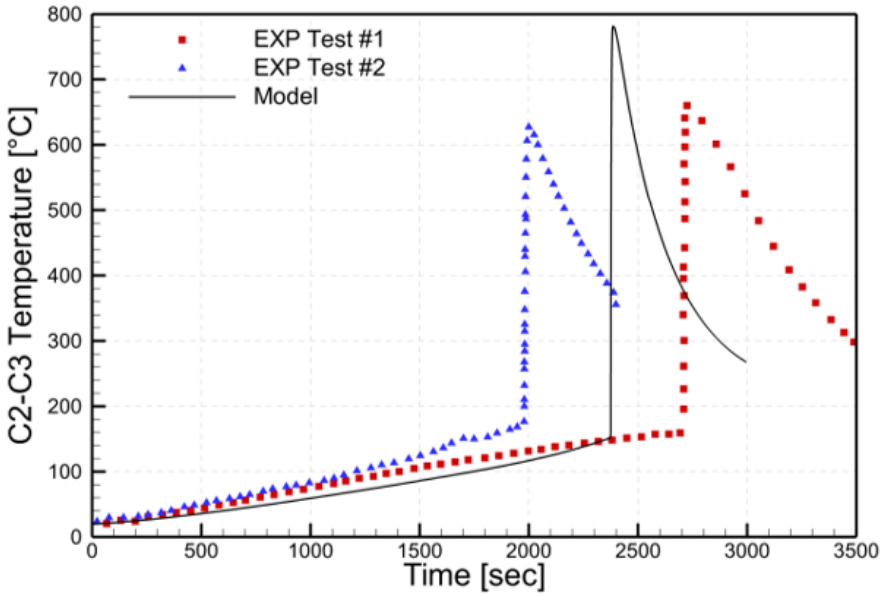

*Figure 31. Comparison between the experimentally measured temperatures (symbols) and that predicted by the electrochemical model (*line*) for the thermal ramp test*

The numerically calculated temperature at the thermocouple placed between the cell 2 and cell 3 is then compared to the two sets of experimentally measured temperatures in Figure 31. In all cases, the temperature of thermocouple slowly increases initially but starts to abruptly rise when the temperature of thermocouple reaches (~160 °C). In the model, thermal runaway happens to start at 2,375 sec, which is in between the thermal runaway start time of test #1 (2,708 sec) and #2 (2,050 sec). The trends of temperature increase and heat dissipations from the numerical model agree well with the two sets of experiments, except for that the current model shows ~110 °C higher maximum temperature.

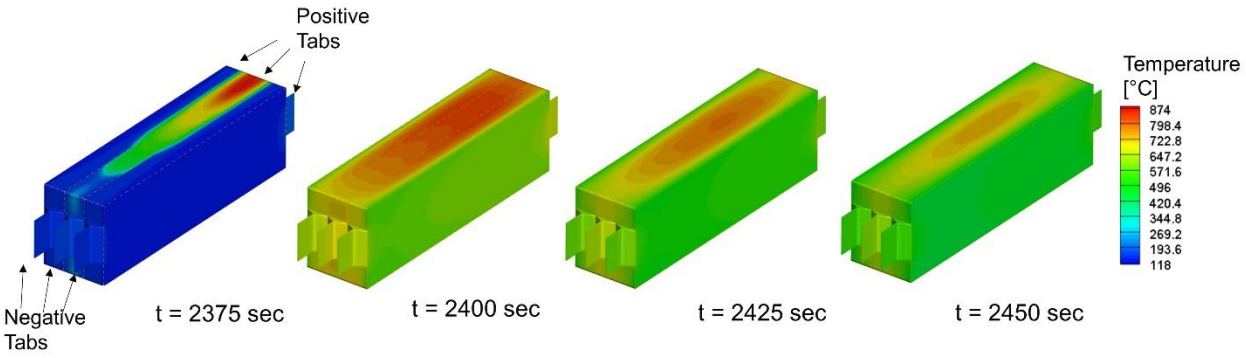

Figure 32. Temperature evolution across the module during the thermal ramp simulations

To understand the damage propagation behavior during the thermal ramp, temporal evolutions of temperature contour from the current numerical model are presented in Figure 32. While the temperature rate during the thermal ramp is slow (5 °C/min), Figure 32 shows that thermal runaway starts to happen first at the region close to positive tab of center cell (cell 2). Two interesting questions arise:

- Why does thermal runaway happen near positive tab first?
- Why does thermal runaway happen at the cell in the center first?

The answer to the first question, is that the positive tab (Al) has 40 percent less volumetric heat capacity than the negative tab (Cu). Also, the tab region heats up faster than the center of the jellyroll region due to larger surface-to-volume ratio. These results will vary in a battery pack, where the busbars are expected to provide additional heat conduction pathways away from the tabs. To answer the second question, cells 1 and 3 heat up slower due to the added thermal mass of the side plates, and thus thermal runaway starts at cell 2 (center) instead of cells 1 or 3. The heat generated from the reactions up to ~120 °C, is absorbed by the side plate attached to cell 1 and cell 3, resulting in a delay of the rapid temperature increase.

4.7. Prediction as a function of model and thermal parameters

There are many parameters that affect the propagation and mitigation behavior of cells undergoing cascading thermal runaway. Outside of the cell design, the primary parameters that an engineer has control over to improve safety are related to heat transfer. There exists a balance between how quickly heat is generated and how quickly it is removed (and where the heat goes). For example, increasing thermal resistance between cells or modules will delay propagation, but mitigation can only be achieved if the delay provides enough time for heat to be removed (i.e. via natural or forced convection, or conduction to structural components).

Before exploration of the heat transfer parameters, it is important to characterize the initiation method, nail penetration in this case, to have a consistent baseline for initiating all exploratory simulations. As the representation of the nail in the quais-1D domain is geometrically different from the true nail, the short circuit model must be adjusted to capture the initiation behavior. Section 4.3 showed the results of refining the short circuit resistance and amount of energy partitioned to the nail. Figure 33 shows the effects of individually perturbing these parameters in the single module case. On the left, the short circuit resistance has been perturbed by ±33 percent. As the heat release rate is inversely proportional to the short circuit resistance, decreasing the short circuit resistance (solid lines) speeds up the initiation of thermal runaway.

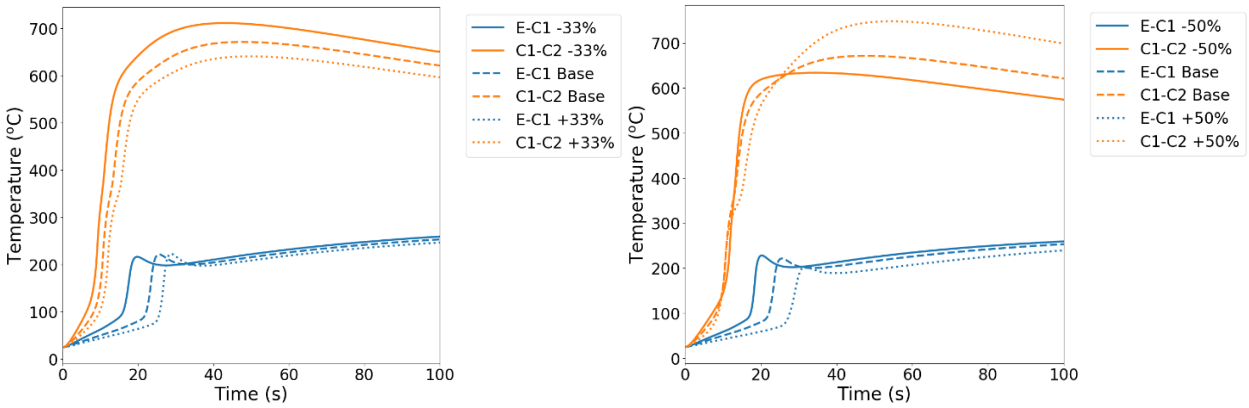

Figure 33. Perturbing the short circuit resistance (left) and fraction of heat deposited in the nail (right)

In Figure 33, above, the fraction of short circuit energy deposited in the nail has been perturbed by ±50 percent. When less energy is deposited in the nail (solid lines), the thermal runaway front propagates faster through the cells adjacent to the nail penetration cell. This is due to greater preheating in the side cells which lowers the energy barrier for initiation of thermal runaway. Conversely, depositing more energy in the nail results in higher peak temperatures at the thermocouple between cells 1 and 2. This is caused by the heat slowly leaving the nail due to relatively low conductivity of the cell compared to the nail.

The addition of spacer plates serves to slow down propagation of thermal runaway through two pathways: by increasing the total heat capacity of the system and creating a delay in the propagation while the plate is heated. The decision to use spacers for mitigation is driven energy density and material cost considerations. Previous work by Torres-Castro et al. (2020) has shown that the addition of increasingly large spacers between each cell will eventually quench thermal runaway. In their investigation, mitigation occurs above approximately a 25 percent increase in heat capacity per total cell mass. In the current work the maximum increase in the effective heat capacity is 14 percent per total cell mass and subsequently mitigation does not occur. However, the increase in effective heat capacity does not take in to account the heterogeneity of the additional heat capacity (i.e. spacers between each cell or sets of cells).

Increasing thermal resistance is the second pathway for mitigation achieved by insertion of spacers. Because the relatively thin plates were less effective in inhibiting propagation for the 1S3P module, we suggest that an approach to heat dissipation that takes advantage of the heat capacity of structural materials might provide enough thermal mass to dissipate the module heat.

Sandia scientists and engineers are carrying out a separately funded study in this area (referred to in this work as the Active Cooling project). The majority of results will be reported elsewhere (Hewson & Kurzawski, in press), but one important observation from the simulation-based design of these Active Cooling experiments is that to allow structural cooling to take place, the heat transfer from the module-to-plate-to-module (the plate configuration in Figure 22 above) needs to be slowed. This can be affected through the addition of a modest amount of insulation materials between cells. The NREL team has a study in section 4.5 combining these effects (insulation plus plates to structural materials and cooling) with good results. Here we analyze the effects of only modest amounts of insulation on the inter-cell and inter-module propagation.

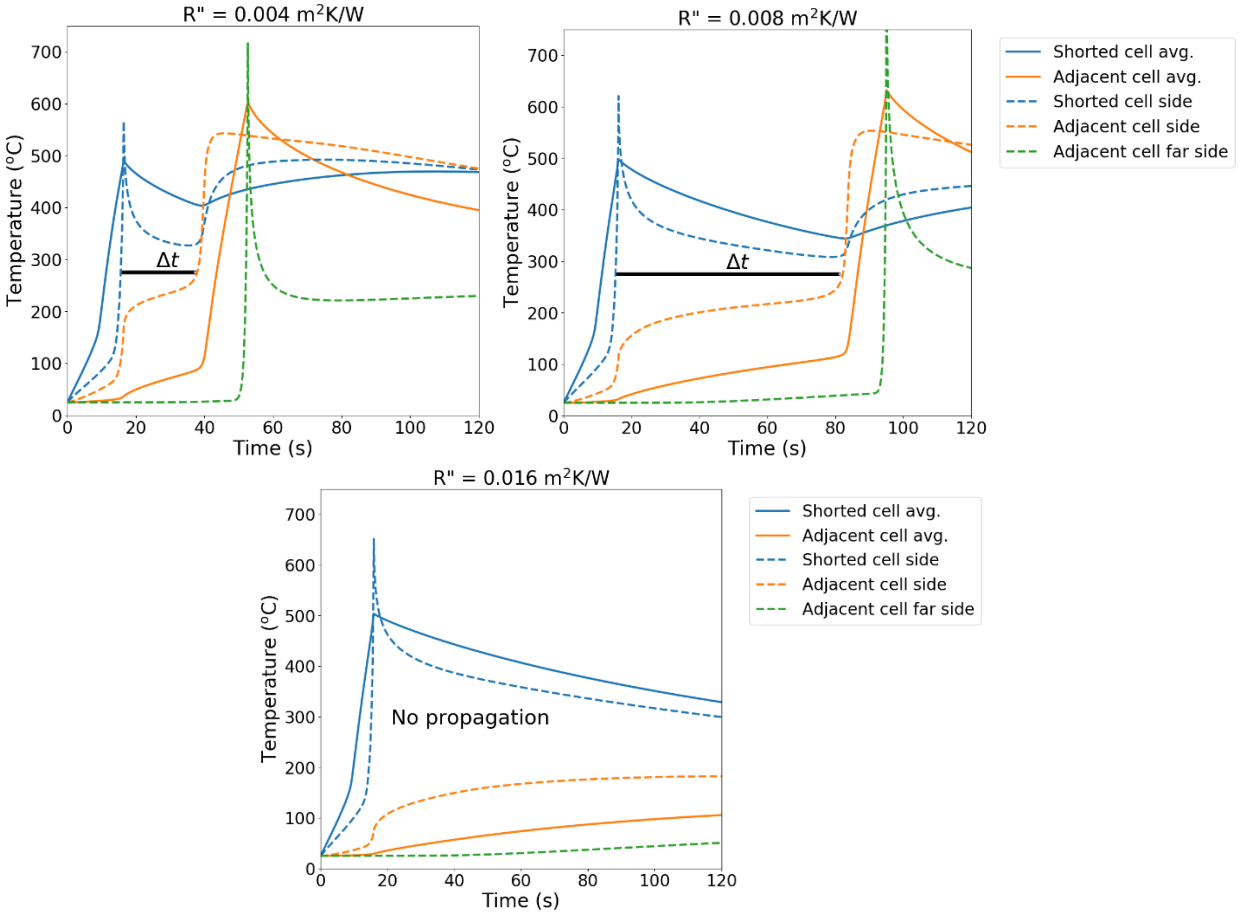

Figure 34. Three 1S1P cells with contact resistance between individual cells. Intercell contact resistances are 0.004 m^2K/W (top left), 0.008 m^2K/W (top right), and 0.016 m^2K/W (bottom). The time lag associated with intercell resistance is indicated with the Δt line.

For simplicity, we enhance the intercell contact resistance to represent the effect of some thermal insulation between cells. This contact resistance neglects the heat capacity of a real insulator, but provides a qualitative assessment of the effect of insulation independent of the previously studied heat capacity effect (Torres-Castro et al., 2020; Li et al., 2019; Kurzawski et al, 2020). This is roughly equivalent to inserting thin, low heat capacity plastic spacers between adjacent cells. As the thermal contact resistance increases, the time lag (Δt) between the shorted cell completing thermal runaway and the adjacent beginning thermal runaway increases. This time lag is

estimated by examining the temperature rise observed at either side of the gap between cells (depicted by dashed lines). An acceleration in the temperature rise (positive curvature) indicates the presence of the thermal runaway front.

Figure 34 shows the effect of adding an enhanced contact resistance between the three cells in a single electrically isolated module (three 1S1P cells). The smallest intercell contact resistance is typical of the mylar pouch cell-to-cell direct contact and there is little delay in the propagation of a failure from one cell to the next. Adding thermal resistance between cells with a magnitude comparable to a mm of plastic insulation causes a strongly increasing delay in the cell-to-cell heating and propagation. These delays are increased from less than 25 s to near 60 s with a 2x increase in the intercell thermal resistance. A large enough thermal resistance will allow cooling to act in a reasonable time. Here we only allow ambient convective cooling, which is generally slow, but doubling the intercell resistance again to four times the original value (0.016 m^2K/W) allows slow convective cooling to the ambient to cease and mitigate propagation. For reference, a thermal contact resistance of 0.016 m2K/W is approximately the same as a 2.5 mm sheet of Mylar.

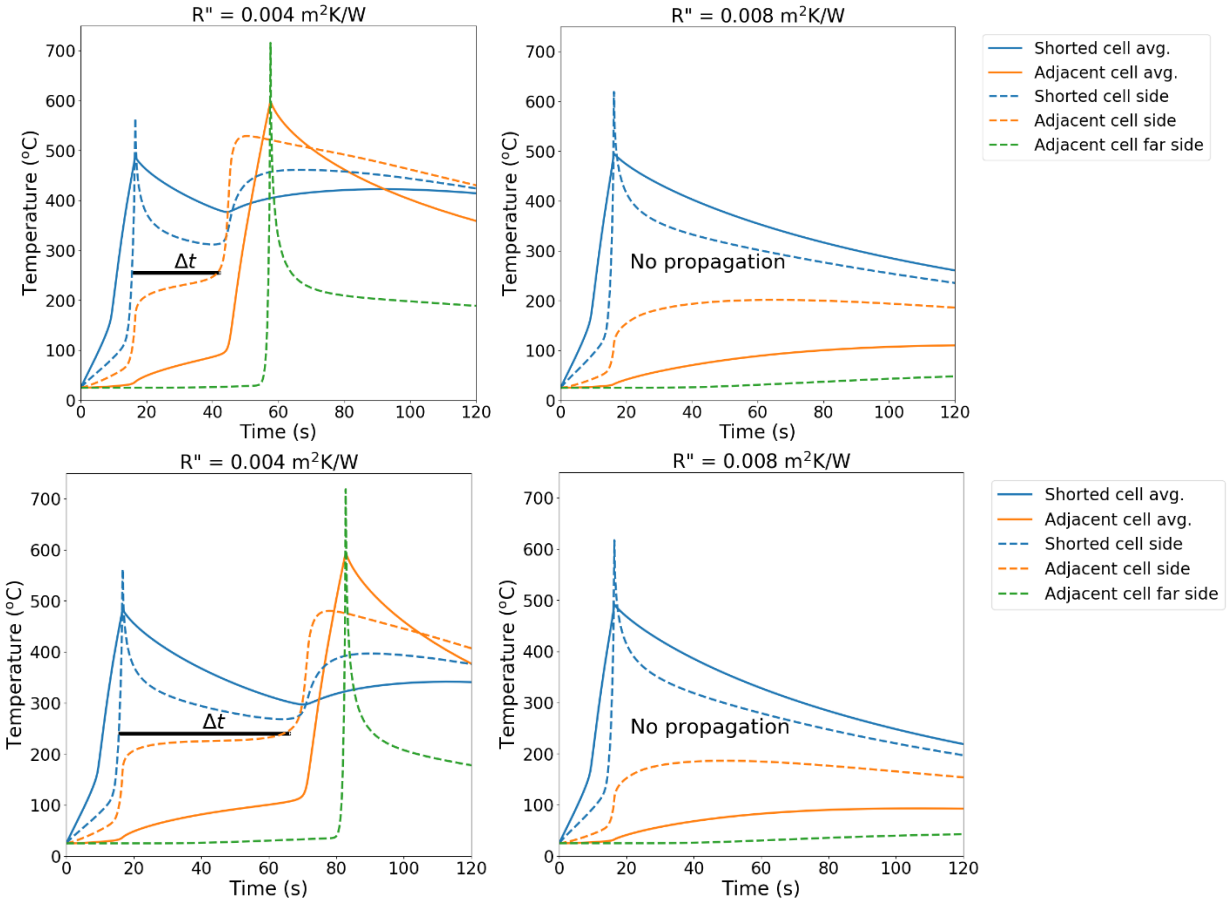

Figure 35. Three 1S1P cells with increased contact resistance between individual cells and increased convective heat transfer to an ambient at 300 K. The left and right panels show intercell contact resistances of 0.004 m^2K/W and 0.008 m^2K/W, respectively. The top to bottom panels show convective heat transfer coefficients of 40 $Wm^{-2}K^{-1}$,and 80 $Wm^{-2}K^{-1}$, respectively. These can be compared to 10 $Wm^{-2}K^{-1}$ in Figure 34. The time lag associated with intercell resistance is indicated with the $\boldsymbol{\Delta t}$ *line.*

The heat transfer coefficient for the simulated cases in Figure 34 employ a convective heat transfer coefficient of 10 $Wm^{-2}K^{-1}$, which is generally on the lower (conservative) side of expected values. If we increase the heat transfer coefficient to the environment (something that mimics heat transfer to structural materials that we present elsewhere) we find that intercell propagation is inhibited at somewhat lower intercell thermal resistances. In Figure 35 we show results with larger heat transfer coefficients that might coincide with forced air convection. For these cases, the combined effect of enhanced convective cooling and increased thermal resistance does mitigate failure propagation; the required increases in both are relatively substantial, however. Creating thermal paths to lose heat to structural materials has a similar effect as increasing the convective heat transfer coefficient (see Sec. 4.5 NREL conductive paths section); the important factor is to remove enough heat from the cell region faster than propagation occurs. We do note that as the system gets closer to the limit of propagation, the sensitivity to both contact resistance and convective cooling should increase. This is observed in the results of Section (4.4 NREL contour) where simulations adding aluminum plates together with the increased contact resistance and convective cooling have a stronger sensitivity to the each of these effects. This occurs because of the strong nonlinearities in the Arrhenius rate constants that are sensitive to changes in the peak temperature, with increasing sensitivity at near-limit conditions.

The previous simulations in Figure 34 and Figure 35 were carried out with three 1S1P cells that were not electrically connected. Electrical connections were removed in this case to isolate all thermal conduction to the areas of direct contact between the cells. As identified before, adding parallel electrical connections allows cells to discharge through the short-circuited cell releasing some heat throughout the system (Lamb et al., 2015). Figure 36 shows the effect of increasing the thermal contact resistance between cells in the 1S3P configuration with electrical connection between the cells. As seen in the top two graphs in Figure 36, a 4x increase in the thermal contact resistance results in an increase in the lag time from 2 seconds to 4.8 seconds, but does not inhibit propagation as occurred for cells that were not electrically connected in Figure 34. This points out some challenges of module level thermal runaway that can be further explored.

While increasing the thermal contact resistance delays propagation between cells, this action has the opposite effect on the propagation time across the adjacent cell. The thermal runaway crossing time for the adjacent cell is estimated by the difference in the sharp temperature rise in the “adjacent cell side” and “adjacent cell far side” lines in Figure 36. This crossing time decreases dramatically as contact resistance increases due to two factors: greater time for pre-heating from the shorted cell and greater time for pre-heating due to joule heating. This phenomenon was also observed in Torres-Castro et al. (2020). When spacers were placed between the shorted cell and adjacent cell, the thermal runaway front propagated through the adjacent cell faster than without spacers. However, in the current work the addition of the electrical connection between the adjacent cells and shorted cell within the module increases the pre-heating of the adjacent cells. This results in the effects of the increasing contact resistance being somewhat less effective in mitigating propagation in electrically connected cells.

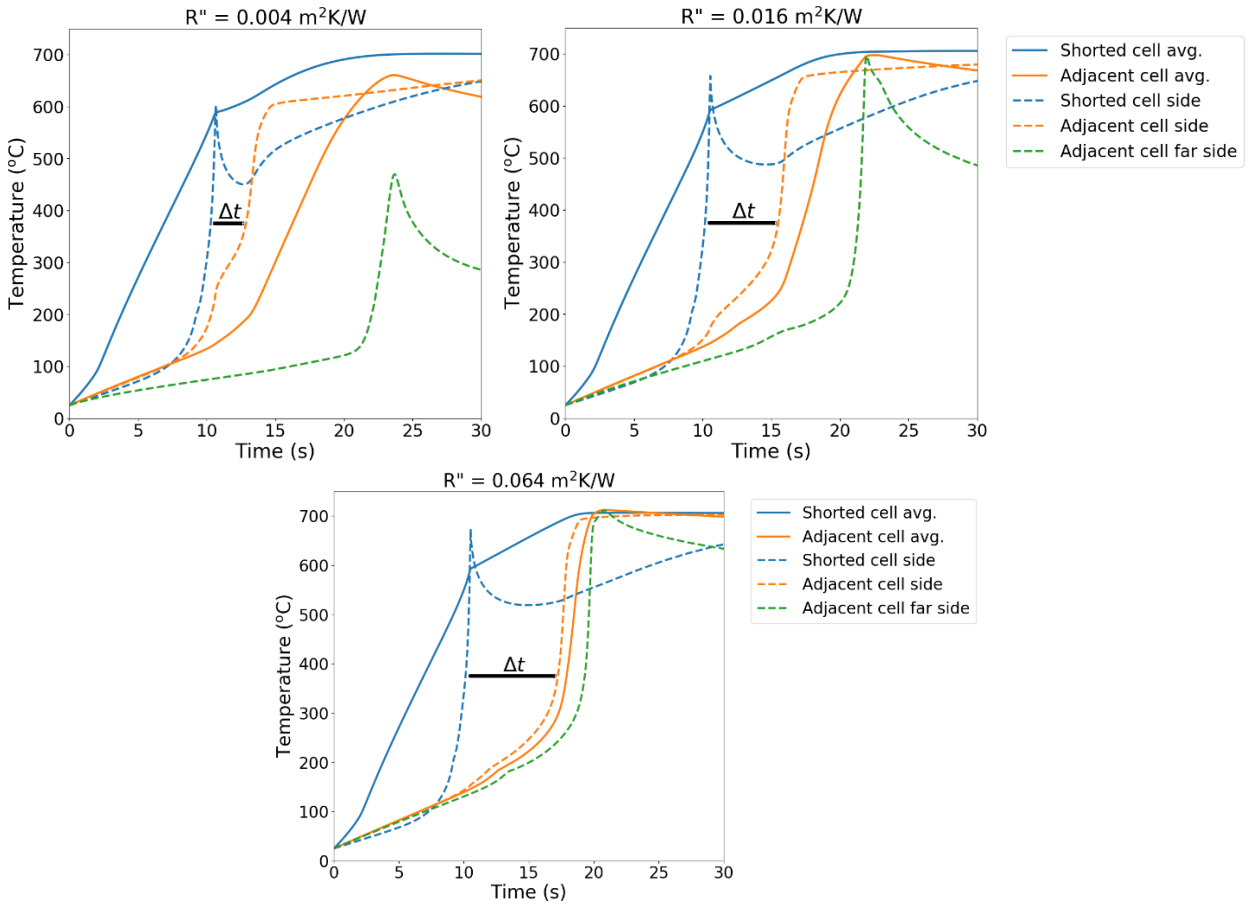

Figure 36. Increasing thermal contact resistance in a 1S3P configuration where cells are electrically connected. The time lag associated with intercell resistance is indicated with the ***Δt*** *line*

4.8. Advanced propagation barrier experiments

Advanced propagation barriers developed as part of this program were analyzed and applied to 1/32" copper plates as a backing material. The following provides comparisons between packs with only 1/32" copper plates and the applied barriers. Figure 37 shows the surface (a) and cross section (b) of the applied barrier. The intended operation is that the embedded copper particles will allow heat conduction during normal and lower temperature failures, preventing excessive heating due to the presence of an insulating material. As temperature increases the matrix material will flow around the particles creating an insulating barrier providing some mitigation to propagating failure.

Figure 38 shows a comparison of thermal runaway propagation failure performed on a 4-cell string of cells with the 1/32" plates alone (a) and with the mitigation barrier applied (b). The data shows that while the engineered barriers did not provide full cell to cell failure mitigation, there were some measurable improvements to the failure behavior. The peak temperatures observed were reduced from 730 °C to 690 °C, and the time to full consumption of the 4-cell string was increased from ~90 seconds to ~130 seconds. This shows the possibility to apply engineered barriers in a way that will dramatically improve the propagation resistance while minimizing

potential weight, volume, and cost increases. The use of a barrier that would be conductive at low temperatures also would allow it to be included as part of an active cooling strategy.

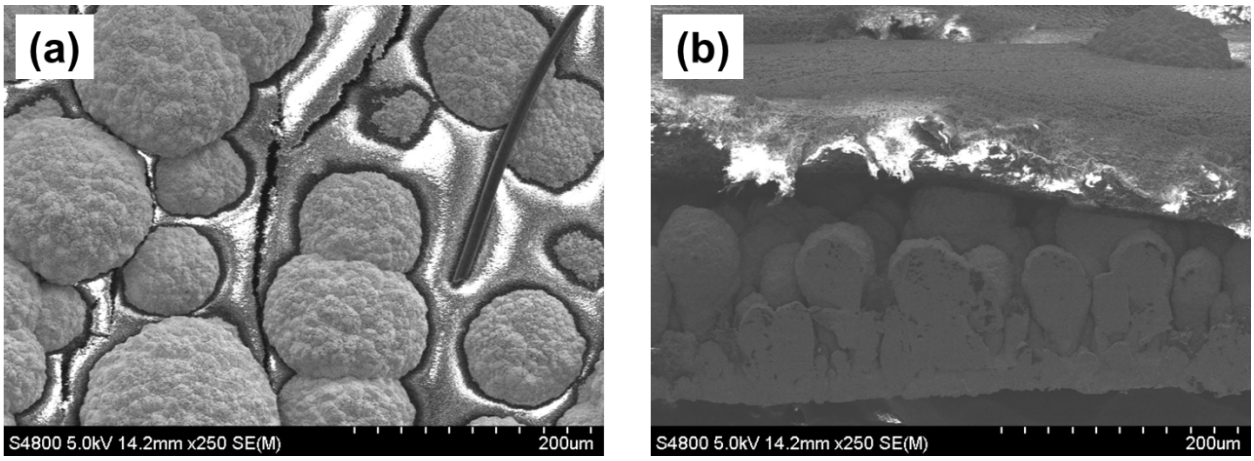

Figure 37. SEM images showing the developed mitigation barriers showing the surface of embedded copper particles (a) and the cross section of the barrier (b). These were applied to 0.0312-inch copper sheets as a backing material with comparisons performed with and without the mitigation barrier.

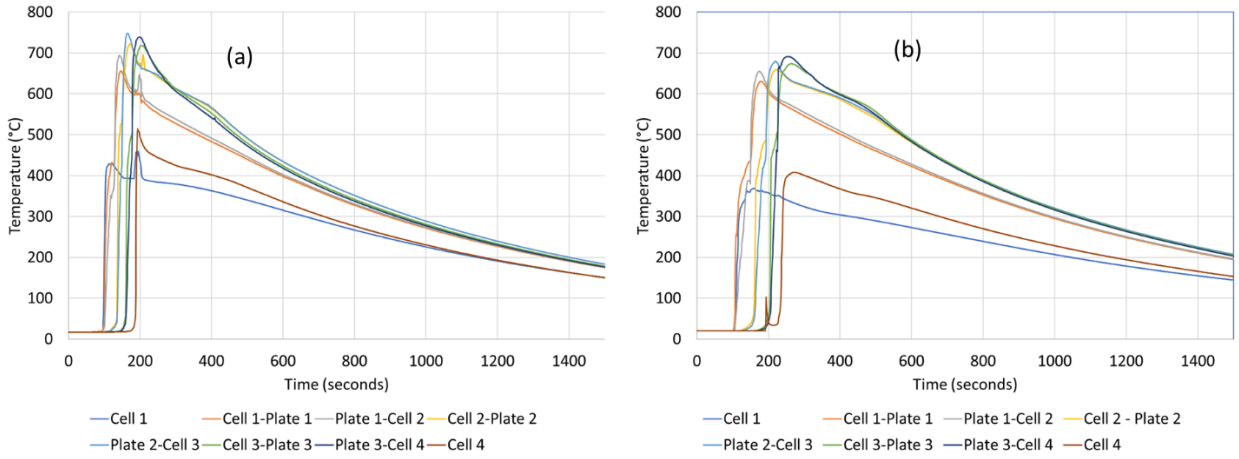

Figure 38. Propagating failure results of 4-cell packs with (a) 0.0312" copper barriers between cells and (b) with 0.0312" copper barriers and engineered membrane between cells

5. References

Ahmed, M. B., Shaik, S., & Jain, A. (2018). Measurement of radial thermal conductivity of a cylinder using a time-varying heat flux method. *International Journal of Thermal Sciences, 129,* 301–308. https://doi.org/10.1016/j.ijthermalsci.2018.03.008

Arbizzani, C., Gabrielli, G., & Mastragostino, M. (2011). Thermal stability and flammability of electrolytes for lithium-ion batteries. *Journal of Power Sources, 196*, 4801–4805. https://doi.org/10.1016/j.jpowsour.2011.01.068

Bandhauer, T. M., Garimella, S., & Fuller, T. F. (2011). A critical review of thermal issues in lithium-ion batteries. *Journal of the Electrochemical Society, 158*. https://doi.org/10.1149/1.3515880

Campion, C. L., Li, W., Lucht, B. L. (2005). Thermal decomposition of LiPF[sub 6]-based electrolytes for lithium-ion batteries. *Journal of the Electrochemical Society, 152.* https://doi.org/10.1149/1.2083267

Crafts, C. C., Doughty, D. H., McBreen, J., Roth, E. P. (2004). *Advanced technology development program for lithium-ion batteries: Thermal abuse performance of 18650 li-ion cells*. Sandia National Laboratories. https://doi.org/10.2172/918751

Dahn, J. R., & Ehrlich, G. M. (2011). Lithium-ion batteries. In T. B. Reddy & D. Linden, eds., *Linden's handbook of batteries, 4th edition.* [Chapter 26]. McGraw-Hill.

Doughty, D. H., Butler, P. C., Jungst, R. G. E.P. & Roth, E. P. (2002). Lithium battery thermal models, *Journal of Power Sources, 110,* 357–363. https://doi.org/10.1016/S0378-7753(02)00198-2

Doughty, D. H., Roth, E. P., Crafts, C. C., Nagasubramanian, G., Henriksen, G., & Amine, K. (2005). Effects of additives on thermal stability of Li ion cells, *Journal of Power Sources, 146,* 116–120. https://doi.org/10.1016/j.jpowsour.2005.03.170

Finegan, D. P., Darcy, E., Keyser, M., Tjaden, B., Heenan, T. M. M., Jervis, R., J.J. Bailey, J. J., Vo, N. T., Magdysyuk, O. V., Drakopoulos, M., Di Michiel, M., Rack, A., G. Hinds, G., Brett, D. L. J., & Shearing, P. R. (2018). Identifying the cause of rupture of li-ion batteries during thermal runaway. *Advanced Science, 5*. https://doi.org/10.1002/advs.201700369

Finegan, D. P., Darst, J., Walker, W., Li, Q., Yang, C., Jervis, R., Heenan, T. M. M., Hack, J., Thomas, J. C., Rack, A., Brett, D. J. L., Shearing, R., Keyser, M., & Darcy, E. (2019). Modelling and experiments to identify high-risk failure scenarios for testing the safety of lithium-ion cells, *Journal of Power Sources, 417*, 29–41. https://doi.org/10.1016/j.jpowsour.2019.01.077

Friel, D. D. (2011). Battery design., In T. B. Reddy & D. Linden, eds., *Linden's handbook of batteries, 4th edition.* [Chapter 5]. McGraw-Hill.

Gu, H. (1983). Mathematical analysis of a Zn / NiOOH cell. *Journal of the Electrochemical Society, 130*, 1459–1464. https://doi.org/10.1149/1.2120009

Guo, M., Sikha, G., & White, R. E. (2011). Single-particle model for a lithium-ion cell: thermal behavior, *Journal of the Electrochemical Society,* 158, A122. https://doi.org/10.1149/1.3521314

Hatchard, T. D., MacNeil, D. D., Basu, A., & Dahn, J. R. (2001). Thermal model of cylindrical and prismatic lithium-ion cells, *Journal of the Electrochemical Society, 148*. https://doi.org/10.1149/1.1377592

Hewson, J. C., & Kurzawski, A. (in press). *Thermal approaches to mitigating cell-to-cell propagation.* Sandia National Laboratories.

Jeevarajan, J. A., Hughes, M. B., Peck, M. S., Tipton Jr., B. C., Bragg, B. J., Piao, T., & Waldrop, S. (1999, October 17 - 22). Performance characterization and safety testing of lithium-ion cells and battery for space flight applications. In S. Surampudi, R. A. Marsh, Z. Ogumi, & J. Prahash, eds., *Lithium batteries: Proceedings of the International Symposium*, 99-25, Honolulu, HI. The Electrochemical Society [2000], pp. 694–705.

Jhu, C. Y., Wang, Y. W., Wen, C. Y., Chiang, C. C., & Shu, C. M. (2011). Self-reactive rating of thermal runaway hazards on 18650 lithium-ion batteries. *Journal of Thermal Analysis and Calorimetry, 106*, 159–163. https://doi.org/10.1007/s10973-011-1452-6

Kim, J., Mallarapu, A., & Santhanagopalan, S. (2020). Transport processes in a Li-ion Cell during an internal short-circuit. *Journal of the Electrochemical Society*. https://doi.org/10.1149/1945-7111/ab995d

Kim, G. H., Pesaran, A., & Spotnitz, R. (2007). A three-dimensional thermal abuse model for lithium-ion cells, *Journal of Power Sources, 170*, 476–489. https://doi.org/10.1016/j.jpowsour.2007.04.018.

Kim, G. H., Smith, K., Ireland, J., & Pesaran, A. (2012). Fail-safe design for large capacity lithium-ion battery systems, *Journal of Power Sources, 210*, 243–253. https://doi.org/10.1016/j.jpowsour.2012.03.015

Kim, G., Smith, K., Lee, K., Santhanagopalan, S., Pesaran, A. (2011). Multi-domain modeling of lithium-ion batteries encompassing multi-physics in varied length scales. *Journal of the Electrochemical Society, 158*(8). https://doi.org/10.1149/1.3597614

Kurzawski, A., Torres-Castro, L., Shurtz, R., Lamb, J., & Hewson, J. C. (2020). Predicting cell-to-cell failure propagation and limits of propagation in lithium-ion cell stacks, *Proceedings of the Combustion Institute, 000*, 1–9. Elsevier. https://doi.org/10.1016/j.proci.2020.06.270

Lamb, J., Orendorff, C. J., Steele, L. A. M., & Spangler, S. W. (2015). Failure propagation in multi-cell lithium ion batteries. *Journal of Power Sources, 283*, 517–523. https://doi.org/10.1016/j.jpowsour.2014.10.081

Lamb, J., Torres-Castro, L., Stanley, J., Grosso, C., & Gray, L. S. (2020). *Evaluation of multi-cell failure propagation* (Report No. SAN D2020-2802). Sandia Laboratories. https://doi.org/10.2172/1605985

Li, Q., Yang, C., Santhanagopalan, S., Smith, K., Lamb, J., Steele, L. A., & Torres-Castro, L. (2019). Numerical investigation of thermal runaway mitigation through a passive thermal management system. *Journal of Power Sources, 429*, 80–88. https://doi.org/10.1016/-j.jpowsour.2019.04.091

Lowy, L. (2013, January 19). Overcharging batteries eyed in Boeing 787 mishaps (Web page). Phys.Org. https://phys.org/news/2013-01-overcharging-batteries-eyed-boeing-mishaps.html

Lu, L., X. Han, X., Li, J., Hua, J., & Ouyang, M. (2013). A review on the key issues for lithium-ion battery management in electric vehicles, *Journal of Power Sources, 226*, 272–288. https://doi.org/10.1016/j.jpowsour.2012.10.060

Mallarapu, A., Kim, J., Carney, K., DuBois, P., Santhanagopalan, S. (2020). Modeling Extreme Deformations in Lithium Ion Batteries, ETransportation. 4 (2020) 100065. https://doi.org/10.1016/j.etran.2020.100065

Musk, E. (2013, October 4). Model S fire, [Blog post]. *Tesla.* www.tesla.com/blog/model-s-fire

Notz, P. K., Subia, S. R., Hopkins, M. M., Moffat, H. K., Noble, D. R., & Okusanya, T. O. (2016, May 2). Sierra Multimechanics Module: Aria User Manual, Version 4.40 (Report No. SAND2016-4159). National Nuclear Security Administration. DOI:10.2172/1262728

Offer, G. J., Yufit, V., Howey, D. A., Wu, B., Brandon, N. P. (2012). Module design and fault diagnosis in electric vehicle batteries, *Journal of Power Sources,* 206, 383–392. https://doi.org/10.1016/j.jpowsour.2012.01.087

Orendorff, C. J., Lamb, J., & Steele, L. A. M. (2017). *Recommended practices for abuse testing rechargeable energy storage systems (RESSs)* (Report No. SAND2017-6925). Sandia National Laboratories. https://doi.org/10.2172/1369524

Ren, F., Cox, T., & Wang, H. (2014). Thermal runaway risk evaluation of Li-ion cells using a pinch-torsion test, *Journal of Power Sources, 249*, 156–162. https://doi.org/10.1016/j.jpowsour.2013.10.058

Richard, M. N., & Dahn, J. R. (1999). Accelerating rate calorimetry studies of the effect of binder type on the thermal stability of a lithiated mesocarbon microbead material in electrolyte. *Journal of Power Sources, 83*, 71–74. https://doi.org/10.1016/S0378-7753(99)00260-8

Roth, E. P. (2019). Abuse response of 18650 li-ion cells with different cathodes using EC:EMC/LiPF6 and EC:PC:DMC/LiPF6 electrolytes. *ECS Transactions, 11*, 19–41. https://doi.org/10.1149/1.2897969

Shurtz, R. C., Engerer, J. D., & Hewson, J. C. (2018a). Predicting high-temperature decomposition of lithiated graphite: Part I. Review of phenomena and a comprehensive model. *Journal of the Electrochemical Society, 165*, A3878–A3890. https://doi.org/10.1149/2.0541816jes

Shurtz, R. C., Engerer, J. D., & Hewson, J. C. (2018b). Predicting high-temperature decomposition of lithiated graphite: Part II. Passivation layer evolution and the role of surface area. *Journal of the Electrochemical Society, 165*, A3891–A3902. https://doi.org/10.1149/2.0171814jes

Shurtz, R. C., & Hewson, J. C. (2020, May 20). Review—Materials science predictions of thermal runaway in layered metal-oxide cathodes: A review of thermodynamics. *Journal of the Electrochemical Society,* 167, 090543. https://doi.org/10.1149/1945-7111/ab8fd9

Spotnitz, , R. M., Weaver, J., Yeduvaka, G., Doughty, D. H., & Roth, E. P. (2007). Simulation of abuse tolerance of lithium-ion battery packs, *Journal of Power Sources,* 163, 1080–1086. https://doi.org/10.1016/j.jpowsour.2006.10.013

Sun, H., Wang, X., Tossan, B., & Dixon, R. (2012). Three-dimensional thermal modeling of a lithium-ion battery pack. *Journal of Power Sources, 206*, 349–356. https://doi.org/10.1016/j.jpowsour.2012.01.081

Tiedemann, W. H., & Newman, J. (1979). Current and potential distribution in lead-acid battery plates. *Proceedings of the Electrochemical Society, 79*(1), 39–49.

Torres-Castro, L., Kurzawski, A., Hewson, J., & Lamb, J. (2020). Passive mitigation of cascading propagation in multi-cell lithium ion batteries, *Journal of the Electrochemical Society,* 167. https://doi.org/10.1149/1945-7111/ab84fa

Troxler, Y., Wu, B., Marinescu, M., Yufit, V., Patel, Y., Marquis, A. J., Brandon, N. P., Offer, G. J. (2014). The effect of thermal gradients on the performance of lithium-ion batteries. *Journal of Power Sources, 247*, 1018–1025. https://doi.org/10.1016/j.jpowsour.2013.06.084

Voelcker, J. (2012, September 24). *Chrysler yanks plug-in hybri test fleet off roads, will replace batteries.* (Web page). Green Car Reports. www.greencarreports.com/news/1079368_chrysler-yanks-plug-in-hybrid-test-fleet-off-roads-will-replace-batteries

Wu, B., Yufit, V., Marinescu, M., Offer, G. J., Martinez-Botas, R. F., & Brandon, N. P. (2013). Coupled thermal-electrochemical modelling of uneven heat generation in lithium-ion battery packs. *Journal of Power Sources, 243*, (544–554. https://doi.org/10.1016/j.jpowsour.2013.05.164

Wu, M. S., Chiang, P. C. J., Lin, J. C., & Jan, Y. S. (2004). Correlation between electrochemical characteristics and thermal stability of advanced lithium-ion batteries in abuse tests - Short-circuit tests. *Electrochimica Acta, 49*, 1803–1812. https://doi.org/10.1016/j.electacta.2003.12.012

Sandia National Laboratories is a multimission laboratory managed and operated by National Technology & Engineering Solutions of Sandia LLC, a wholly owned subsidiary of Honeywell International Inc. for the U.S. Department of Energy's National Nuclear Security Administration under contract DE-NA0003525.

The modeling work at the National Renewable Energy Laboratory (NREL) was supported by US Department of Transportation, NHTSA under Contract# DOT IAG-18-2082. The research was performed using computational resources sponsored by the Department of Energy's Office of Energy Efficiency and Renewable Energy, located at the National Renewable Energy Laboratory. The U.S. Government retains and the publisher, by accepting the article for publication, acknowledges that the U.S. Government retains a nonexclusive, paid up, irrevocable, worldwide license to publish or reproduce the published form of this work, or allow others to do so, for U.S. Government purposes.

DOT HS 813 230
March 2022

U.S. Department
of Transportation

**National Highway
Traffic Safety
Administration**

15471-120921-v1a